The Japan Society of Applied Physics

PROGRESS REVIEW

Ca silicide films—promising materials for silicon optoelectronics

View the article online for updates and enhancements.

Ca silicide films—promising materials for silicon optoelectronics

Nikolay G. Galkin[1*] , Konstantin N. Galkin[1], Dmitrii L. Goroshko[1], Sergei A. Dotsenko[1], Oleg V. Kropachev[1] , Igor M. Chernev[1], Evgenii Yu Subbotin[1], Aleksey Yu Alekseev[2], Dmitry B. Migas[2], Zsolt Fogarassy[3], Bela Pecz[3], and Anton K. Gutakovskii[4]

[1]Laboratory of Optics and Electrophysics, Institute of Automation and Control processes FEB RAS, 5, Radio Str., 690022, Vladivostok, Russia
[2]Belarusian State University of Informatics and Radioelectronics, 220013 Minsk, Belarus
[3]Energy Research Institute, 1525 Budapest Pf, 49, Hungary
[4]Rzhanov Institute of Semiconductor Physics SB RAS, Novosibirsk, 630090, Russia

*E-mail: galkin@iacp.dvo.ru

Single-phase films of semiconductor and semimetallic calcium silicides (Ca_2Si, $CaSi$, and $CaSi_2$), as well as films with a significant contribution of Ca_5Si_3 and $Ca_{14}Si_{19}$ silicides, were grown on single-crystal silicon and sapphire substrates. The analysis of the crystal structure of the grown films was carried out and the criterion of their matching with silicon and sapphire substrates was determined. Some lattice-matching models were proposed, and the subsequent deformations of the silicide lattices were estimated. Film's optical functions, including the optical transparency, were calculated from the optical spectroscopy data and an extended comparison was performed with the results of ab initio calculations. The real limits of the optical transparency for the films on sapphire substrates were established. The maximum transparency limit (3.9 eV) was observed for the CaSi film. Based on an analysis of the photoelectric properties of Ca_2Si/Si diodes on n- and p-type silicon substrates, a perspective of their applications in silicon optoelectronics was discussed. © 2022 The Japan Society of Applied Physics

1. Introduction

Semiconductor silicides of alkaline Earth metals (Ca, Mg, Ba), including their ternary compounds, attract considerable attention as materials for thermoelectric converters, photodiodes and LED.[1–4] Among these elements, calcium (Ca) is one of the most common elements in the Earth and occupies the 5th place in their total distribution.[5] Calcium silicides form six compounds Ca_2Si, $CaSi$, Ca_5Si_3, Ca_3Si_4, $Ca_{14}Si_{19}$, and $CaSi_2$ with different crystal structures and compositions and have a wide range of properties from semiconductor to semimetallic, including both bulk and layered structures, with promising properties for semiconductor conductivity, thermoelectricity and biological applications.[6–12] Theoretical studies were mainly focused on semiconductor silicides (Ca_2Si and Ca_3Si_4),[7,8,13–18] whereas calcium semi-silicide (Ca_2Si) attracted experimental attention.[19–22] According to the first principal calculations, Ca_2Si is a direct-gap semiconductor with a band gap from 0.30–0.36 to 1.02 eV indicating a possibility to fabricate on silicon light-emitting diode structures in the near-infrared range.[13–16,18] However, the direct-gap band nature has not yet been confirmed by experimental data due to difficulties in implementing the epitaxial growth of Ca_2Si on silicon and in determining the fundamental transition under conditions of high defect density of Ca_2Si film and weak transparency of a silicon substrate at photon energies smaller 1.1 eV.[21] Semiconductor epitaxial Ca_2Si films on a Si(111) substrate were recently grown through the formation of a two-dimensional (2D) sacrificial Mg_2Si layer with the following transformation into 2D Ca_2Si and then the growth to thick Ca_2Si films by MBE at 250 °C.[21,23,24] A little later, it was established that the phase composition of the grown Ca_2Si film depended on the ratio of calcium to silicon deposition rates, and at this ratio of 4.0, a single-phase film grew with the $Ca_2Si(100)$/Si(111) epitaxial ratio.[25] For the growth of Ca_2Si films on Si(001) and Si(110), the aforementioned sacrificial layer technique based on the 2D Mg_2Si layer was also used for the first time, followed by its transfer to the Ca_2Si seed layer at 250 °C in a Ca flow

and growth by MBE at 300 °C.[23–25] It has been established that in a 140 nm thick film at the low 4.7 ratio of Ca to Si fluxes, three silicides are formed simultaneously: Ca_2Si, $CaSi$, and $hR3-CaSi_2$. At the same time, a decrease in the MBE growth temperature to 250 °C and an increase in the ratio of Ca to Si fluxes to 8.4 made it possible to form a polycrystalline Ca_2Si film with a minimal contribution of CaSi.

For thick epitaxial and polycrystalline Ca_2Si films grown on Si(111), Si(110), and Si(001) substrates, peak positions in the reflection and Raman spectra and absorption peaks in the far-IR spectra were determined and identified for the first time.[21,25] A direct interband transition was found in Ca_2Si films at 1.095 ± 0.1 eV with a noticeable oscillator strength, and it was found that the fundamental transition in Ca_2Si films is masked by the Urbach edge in the photon energy range 0.78–1.0 eV and retained absorption below 0.7 eV due to scattering at grain boundaries.[25,26] It has been established that the last range (below 0.6 eV) correlates with the beginning of the region of the dispersionless refractive index for an epitaxial Ca_2Si film (n_o = 3.53),[21] while a small amount of the CaSi phase in polycrystalline Ca_2Si films on Si(110) and Si(001) does not affect absorption at photon energies below 0.4 eV.[25] In Ca_2Si films, due to their epitaxial growth on a silicon substrate with its limited transparency above 1.12 eV, it turned out to be impossible to determine the fundamental absorption edge below 1 eV.[26] For the first time, a nanocrystalline (NC) Ca_2Si film was grown on a transparent $Al_2O_3(0001)$ substrate with sequential formation of an amorphous 2D Si layer, a sacrificial 2D Mg_2Si layer and a Ca_2Si seed layer.[23,24,27] One $Ca_2Si(211)$/$Al_2O_3(0001)$ epitaxial relationship was found in this NC film. Moreover, individual CaSi nanocrystals were detected as well with the $CaSi(001)$/$Al_2O_3(0001)$ relationship. Studies of the optical properties and parameters of the band structure of Ca_2Si on sapphire revealed a direct fundamental transition of 0.88 ± 0.01 eV in addition to three more direct interband transitions of 1.16, 1.49, and 1.61 eV with appreciable oscillator strength.[27] At photon energies

from 0.78 to 0.88 eV, the main contribution to absorption is due to the Urbach tail on defects in Ca_2Si nanocrystals, while absorption at grain boundaries occurs at photon energies from 0.6 to 0.78 eV.[26] It is also assumed that the contribution of the CaSi phase is associated with absorption by free carriers injected into the Ca_2Si film at photon energies below 0.6 eV.

Since theoretical[13–16,18] and experimental[21,25,27] investigations of semiconductor Ca_2Si have revealed its complex electronic structure, the temperature dependences of the spectral photoconductivity were studied for the first time in the temperature range from 10 to 300 K to confirm the photogeneration of carriers and determine the nature of the interband transition in the Ca_2Si epitaxial film grown on a Si (111) substrate.[28] Since the red boundary in the photoconductivity spectrum is proportional to the absorption coefficient and depends on the energy position of the fundamental interband transition,[26] using three thermodynamic models, the existence of a direct fundamental transition with E_g = 1.195 eV at 0 K was established, and the experimental dependence $E_g(T)$ was plotted.[29–31] This interband transition at 300 K (1.163 eV) is close to the value (1.195 eV) determined at 300 K from optical spectroscopy data.[21,25,27] In addition, the effective phonon energy ($\langle E_{ph} \rangle$ = 48.3 ± 1.8 meV), the dimensionless electron–phonon coupling constant (S = 1.819 ± 0.17), the Einstein (Ξ = 561 K) temperature, and the hole mobility μ = 98 cm^2 V^{-1} × s^{-1} at room temperature were determined.

The low-temperature electronic and lattice properties of bulk CaSi and $CaSi_2$ polycrystals have been studied by measuring the specific heat, resistivity, Hall effect, and magnetoresistance.[32] Thus, an analysis of the magnetotransport properties has shown that at 273 K these polymorphs are compensated metals and the calculated carrier density for $CaSi_2$ is an order of magnitude higher than for CaSi. In accordance with calculations of the electronic band structure, the authors concluded that the Ca d-electrons play a dominant role in charge transfer.[32] It is experimentally estimated that the Debye temperature for $CaSi_2$ is higher than for CaSi, which corresponds to an increase in the Ca–Si interaction with Si concentration.[32] In these works,[33–36] in amorphous, nanocrystalline (NC), and polycrystalline films of calcium mono- and disilicide (CaSi and $CaSi_2$) grown on high-resistivity silicon substrates with (111) and (100) orientations, the relationship between the structure, grain morphology, optical properties, and parameters of the band structure, low-temperature Hall and magnetoresistive effects, as well as high-temperature thermoelectric generation of carriers is revealed. Low-temperature Hall measurements showed that all the studied systems were characterized by a predominant contribution of holes in the range 1.4–300 K.[35] For CaSi films with an additional $CaSi_2$ phase, a giant linear magnetoresistive effect (MRE, 200%–500%) occurred in magnetic fields of 1–4 T at T = 40–100 K. In a single-phase $CaSi_2$ film, this MRE effect was not detected in the temperature range from 50 to 250 K pointing out that there was a certain rearrangement in the magnetic field of carrier fluxes in a two-phase system. The semimetallic type of conductivity in CaSi and $CaSi_2$ films is accompanied by the positive Seebeck coefficient at T = 330–450 K.[35] The maximum Seebeck coefficient and power factor are observed in the case of a single-phase amorphous CaSi film with a

certain fraction of the Ca_2Si NC phase. In the case of a single-phase polycrystalline $CaSi_2$ film with two polytypes of the same orientation [hR3-$CaSi_2$(001) and hR6-$CaSi_2$(001)], the Seebeck coefficient and the power factor are halved.

$CaSi_2$ can be viewed as a platform to form silicene layers —2D silicon layers with a deformed buckled structure close to graphene, which can be a new-generation 2D Dirac thermoelectric material that is superior to traditional layered thermoelectric materials.[37,38] First of all, homogeneous and high-quality hR6-$CaSi_2$ films with a thickness of 59 nm were successfully grown by co-deposition of Ca and Si on a Si (111) substrate at a temperature of 560 °C.[37] However, the optical, electrical, and thermoelectric properties of the data films have not been studied. A new technique has been proposed for intercalation of Ca atoms into epitaxial $CaSi_2$ films, which not only deformed the silicene buckled structure but also retained the metal-like electrical conductivity with a simultaneous three-fold increase in the Seebeck coefficient, providing an increase in the thermoelectric figure of merit.[38] In the next work, an oriented single-phase film was grown with the hR6-$CaSi_2$ structure on the Si(111) substrate, which showed semi-metallic properties with a low magnetoresistance effect of 27% at 2 K in the magnetic field of 8 T, low charge carrier mobility ~(2–50) cm^2 × V^{-1} × s^{-1} in the temperature range of 2–300 K, the absence of a semimetal–semiconductor transition and saturation of the magnetoresistance to 2 K at 8 T, which is due to close to ideal carrier compensation.[39]

The most important factor that was previously discovered in polycrystalline $CaSi_2$ films is a combination of high conductivity and sufficiently high transparency in the IR range.[39–41] In fact, a relatively thick (130 nm) hR6-$CaSi_2$ film was characterized by an optical transparency no worse than 20% in the NIR and MIR spectral ranges, reaching a transmittance of 47% at a wavelength of 1550 nm and maintaining a low specific electric (87 $\mu\Omega$ × cm) and sheet (6.6 $\Omega/\square$) resistances at room temperature.[39–41] It has been shown that hR6-$CaSi_2$ films on silicon, having a high standardized quality factor of 0.2 Ω^{-1}, are suitable for silicon-based optoelectronics, competing with other modern transparent conductive materials, such as ITO (indium-tin oxide).[42,43] The $CaSi_2$ film grown on a sapphire substrate demonstrated optical transparency in the visible region.[39]

For Ca_5Si_3 only scarce and sometimes contradictory data can be found in literature. Based on a limited amount of experimental data for porous Ca_5Si_3 synthesized in a Ca flow on a Si substrate, a narrow gap (<50 meV) has been detected, but the temperature dependence of the effective electronic conductivity displayed anomalies.[44] At the same time, ab initio calculations for Ca_5Si_3 revealed transitions from a semi-metallic to a semiconductor character depending on the geometric relaxation of the structure.[44] Ca_5Si_3 demonstrated a metallic temperature dependence of the electrical conductivity on samples sintered by arc welding in the range of 2–300 K, which was inconsistent with the data of the work.[44] The other combined experimental and theoretical study of the Ca_5Si_3 phase was also conducted.[45] The density of states and band structure of Ca_5Si_3 was calculated by first-principles methods indicating the metallic ground state with a peak in the density of states below the Fermi energy and a sharp minimum directly above it.[45] For the first time, Ca_5Si_3 films

were formed on a Si(100) substrate using a system of radio frequency (RF) magnetron sputtering (MS) and subsequent preliminary annealing at 600 °C for 2 h.[46] It has been established that additional vacuum annealing in the temperature range of 750 °C–800 °C leads to the formation of a cubic Ca_2Si film with a band gap of 0.385 eV according to optical spectroscopy data.[46] The formation of a Ca_5Si_3 film (according to X-ray diffraction data) was observed during vacuum annealing at $T = 850$ °C.[46] An analysis of the transmission and reflection spectra showed that the Ca_5Si_3 films have semiconductor properties with a direct band gap of 0.65 eV,[46] which also contradicts the published data.[45]

It turned out that rhombohedral $Ca_{14}Si_{19}$ was only formed as bulk samples. Thus, the peritectic reaction was used to fabricate $Ca_{14}Si_{19}$ displaying a new type of 2D silicon framework formed by 3,3,3-barrelanes Si_{11} linked by Si_3 bridges, leaving room for interstitial calcium atoms.[47] The thickness of such 2D silicon layers is about 0.80 nm. $Ca_{14}Si_{19}$ was also obtained by sintering in an induction furnace in a closed crucible from stoichiometric mixtures of Ca and Si powders, followed by their homogenization from sealed quartz ampoules in argon at $T = 1333$ K for 25 d.[48] Arc melting in an argon atmosphere, using Ca pellets (99.5%) and pieces of silicon (99.999%), was applied to form $Ca_{14}Si_{19}$ indicating that the homogeneity of the samples was improved by double re-melting.[49] The temperature dependences of the heat capacity were measured in the temperature range of 3–300 K by the adiabatic calorimetry, which exhibited at $T < 40$ K a power law with an exponent less than three due to the layered structure.[48] The transport properties of $Ca_{14}Si_{19}$ were not studied.[47,48] The Seebeck coefficient for $Ca_{14}Si_{19}$ (-183 μV deg^{-1}) was estimated at room temperature.[49] Ab initio calculations revealed that $Ca_{14}Si_{19}$ is a semiconductor with a band gap of 0.1 eV.[47] In addition, the first-principles calculations were used to analyze experimental Raman spectra and optical vibrational spectra on bulk $Ca_{14}Si_{19}$ samples with electrons as the majority carriers.[49]

The analysis of the growth and properties of Ca silicides with different compositions and crystal structures showed that film growth was most realized for $CaSi_2$, Ca_2Si, and $CaSi$ with the simplest structure and potentially interesting optical, electrical, and thermoelectric properties. Contrary, silicides with a more complex crystal structure, such as Ca_3Si_4, Ca_5Si_3 and $Ca_{14}Si_{19}$, have very limited experience in the implementation in the form of films (Ca_5Si_3,[43–45]), double heterostructure (Ca_3Si_4,[50–52]) or do not have it at all ($Ca_{14}Si_{19}$,[47–49]) due to complex peritectic reactions of their formation and similar formation energies,[6] which extremely complicates the single-phase and oriented growth of these silicides on single-crystal silicon and other substrates. In general, this also applies to all Ca silicides, but for Ca_2Si[21,25,27] and $CaSi_2$ [25,27,37–39] these growth problems are generally solved, either by using the original technique of the sacrificial seed layer,[23,24] or by a selection of kinetic growth parameters.[25,37] However, the problem of single-phase growth of CaSi has not been completely solved.[34,35] In addition, the problem of studying the crystal structure and optical transparency in single-phase CaSi and Ca_2Si films, both on silicon and sapphire substrates, remains unresolved, and in comparison with the optical transparency of $CaSi_2$ films. To solve it, one can use the calculations of the densities

of states from optical spectroscopy data and compare them with data on the electronic structure and optical properties from first-principle calculations. Approaches to the growth of Ca_5Si_3 and $Ca_{14}Si_{19}$ films on silicon and sapphire have not been developed, and their optical properties and phonon structure have not been studied.

The objectives of this work were: (i) to fill in the missing information on the growth, crystal structure, and detailed optical characterization of single-phase epitaxial Ca_2Si, $CaSi_2$ (with different types of crystal structures),[37,53] and CaSi films on silicon and sapphire substrates; (ii) development of approaches to the growth of silicide films with a more complex crystal structure, such as Ca_5Si_3 and $Ca_{14}Si_{19}$; (iii) study of their matching with the crystal lattice of silicon; (i–iv) determination of their optical functions, including optical transparency; (i–v) carrying out first-principles calculations of the optical functions of semiconductor and semimetallic calcium silicides and comparison with experimental data; and (i–vi) analysis of the prospects of using thin semiconductor Ca_2Si films to fabricate silicon-silicide diode structures.

2. Experimental methods

All experiments on the formation of Ca silicide films on single-crystal silicon and sapphire ($Al_2O_3(0001)$) were carried out in OMICRON Compact and VARIAN ultrahigh-vacuum setups with a base vacuum of 1×10^{-10} Torr, equipped with a LEED and AES/EELS analyzer, and a block of Si, Ca and Mg molecular-beam sources and a quartz thickness gauge. The Si source in both growth chambers was a rectangular strip of silicon (4×17 mm^2) with p-type conductivity and a resistivity of 1000 $\Omega \times$ cm. Rectangular silicon strips with (111), (100) and (110) orientations (5.0×17 mm^2) of p- or n-type conductivity with resistivity from 45 to 1000 $\Omega \times$ cm were used as substrates. As sources of Mg and Ca, we used Knudsen cells made of pyrolytic boron nitride when heated by direct current. CaSi and $CaSi_2$ films were grown on silicon and sapphire substrates using the sacrificial-template method, which is described in detail elsewhere, with the selection of magnesium, calcium, and silicon deposition rates.[21,27] CaSi and $CaSi_2$ films were grown on both types of substrates using reactive deposition epitaxy (RDE) and molecular-beam epitaxy (MBE) methods with the selection of the substrate temperature, Ca deposition rate, and the ratio of Ca to Si fluxes to implement single-phase growth during MBE growth.[34,36,40] Growth of calcium silicides on silicon and sapphire with structures Ca_5Si_3 and $Ca_{14}Si_{19}$ were carried out according to the original method through the formation of calcium monosilicide (by MBE or RDE methods) followed by an increase in the amount of Ca by RDE with the selection of the substrate temperature from 500 °C to 700 °C to convert CaSi to Ca_5Si_3 or $Ca_{14}Si_{19}$. The growth parameters of the Ca silicide films used and its crystal structures are shown in Table I.

After unloading samples from the UHV chamber, the crystal structure and optical properties of grown Ca silicide films, were investigated and analyzed, using the methods of transmittance electron microscopy, X-ray diffraction, optical spectroscopy and Raman spectroscopy yearly ourselves described.[21,25,27,34,36,41,52] Calculations of the optical functions of Ca silicide films on silicon and sapphire substrates were carried out from the transmission and reflection optical

Table I. Growth parameters and structure of samples with Ca silicide films on Si and sapphire substrates (silicide film thicknesses were determined by cross-section TEM or from Ca and Si deposition rates, deposition time, and expected Ca accommodation coefficient).

Sample	Substrate	Deposited materials	Deposition rate: v_{Mg}, v_{Ca}; v_{Si} (nm min^{-1})	Substrate temperature (°C)	Deposition time (min)	Silicide thickness (nm)	TEM or XRD data
						Ca$_2$Si on Si(111)	
A	Si(111)	Mg	0.75	150	1		TEM (cr. sec.) Ca$_2$Si[010]//Si[$\bar{1}$12]
		Ca	0.1	300	10	142–150(TEM)	XRD
		Ca + Si	(8.4 + 0.4)	300	60		Ca$_2$Si (400)/Si(111)
B	Si(111)	Mg	0.75		1		TEM (cr. sec.) Ca$_2$Si[010]//Si[$\bar{1}$12]
				150		147–168 (TEM)	XRD
		Ca	0.1	250	20		Ca$_2$Si(220)//Si(111)
		Ca + Si	(5.8 + 0.8)	250	10		Ca$_2$Si (301)/Si(111)
						Ca$_2$Si on sapphire	
C	Al$_2$O$_3$(0001)	Si	0.9	30	12		XRD
		Mg	0.4	150	1	10	
		Ca	0.1	300	20	95	Ca$_2$Si (422), CaSi(002)
		Ca + Si	(7.5 + 0.9)	250	30		
						CaSi on Si(111)	
D	Si(111)	Mg	0.4	100	1	95–105 (TEM)	TEM (cr. sec.) CaSi(220)‖Si(111)
		Ca	0.1	250	10		CaSi[001]‖Si[$\bar{1}$10]
		Ca + Si	(2.0 + 0.45)	300	10		CaSi[00 $\bar{1}$]‖Si[$\bar{1}$10] XRD
		Ca + Si	(2.0 + 0.45)	400	10		CaSi(330)//Si(111)
		Si	0.45	30	10		CaSi(220)//Si(111)
E	Si(111)	Ca	7.0	475	10	130	XRD CaSi(200)//Si(111) CaSi(020)//Si(111)
						CaSi on sapphire	
F	Al$_2$O$_3$(0001)	Si	0.88	30	10	70	XRD
		Ca + Si	(2.7 + 0.9)	470	20		CaSi(020), CaSi(024)
						CaSi$_2$ on silicon	
G	Si(001)	Ca + Si	(0.9 + 0.4)	500	24		TEM (cr. sec.) hP3-CaSi$_2$[100]//Si[110]
			0.4				
						15 (TEM)	XRD hP3-CaSi$_2$(010)‖Si(002) hP3-CaSi$_2$[100]‖Si[110] hP3-CaSi$_2$[001]‖Si[1$\bar{1}$0]
		Si		30	10		
H	Si(001)	Ca + Si	(8.3 + 0.3)	680	100	382 (TEM)	TEM (cr. sec.) Two grains: hR6-CaSi$_2$[100]‖Si[1$\bar{1}$0] hR6-CaSi$_2$(01$\bar{1}$)‖Si(002) XRD hR6-CaSi$_2$(012)//Si(001)
J	Si(111)	Ca + Si	(7.3 + 0.95)	500	10	70	XRD hR6-CaSi$_2$(006)//Si(111)
						CaSi$_2$ on sapphire	
K	Al$_2$O$_3$(0001)	Ca + Si	(2.0 + 0.8)	660	60	60	XRD hR6-CaSi$_2$(110) //a-Al$_2$O$_3$(0001)

Table I.   Continued.

Sample	Substrate	Deposited materials	Deposition rate: v_{Mg}, v_{Ca}; v_{Si} (nm min^{-1})	Substrate temperature (°C)	Deposition time (min)	Silicide thickness (nm)	TEM or XRD data
				Ca_5Si_3 + CaSi on Si(100)			
L	Si(001)	Ca + Si	(0.9 + 0.3)	400	30		XRD
		Ca	1.5	490	5		Ca_5Si_3(004)//Si(001)
		Ca	1.5	600	5		CaSi(021)//Si(001)
		Ca	1.5	700	5		
				Ca_5Si_3 + CaSi + hR6-CaSi$_2$ on sapphire			
M	Al$_2$O$_3$(0001)	Ca + Si	(4.0 + 0.7)	470	180	240	XRD
							Ca_5Si_3(121), CaSi(110),
							hR6-CaSi$_2$(003)//a-Al$_2$O$_3$(0001)
				Ca_5Si_3 + CaSi + hR3-CaSi$_2$ on Si(111)			
N	Si(111)	Ca	0.68	500	10	10	XRD
		Ca + Si	(1.4 + 0.67)	500	100	180	hR3-CaSi$_2$(003)//Si(111)
							CaSi(020)//Si(111)
							Ca$_{14}$Si$_{19}$(4 $\bar{2}$0)//Si(111)

spectra in the framework of a two-layer model or from the reflection spectra in the photon energy range 0.04–6.5 eV using the integral Kramers–Kronig relations.[26,54]

In this work, full structural optimization for all selected Ca silicides was carried out from first-principles using the total energy method, which was supplemented by a wave projector (WASP code).[55–58] For calculations, both the generalized gradient approximation (GGA) of Perdue–Burk–Ernzerhoff and the screened hybrid functional of Heyd, Scuseria and Ernzerhoff (HSE) with standard settings of screening and Hartree–Fock mixing parameters.[59–65] The calculations were performed by implementing the energy cutoff of 320 eV and the Monkhorst–Pack grids of $13 \times 13 \times 9$ (for GGA) and $6 \times 6 \times 2$ (for HSE). Structural optimization was stopped when the forces acting on the atoms were less than 0.01 eV Å^{-1}. The total energy convergence was better than 1 meV atom^{-1}.

For the sake of optical functions comparison between theory and experiment, we selected Ca_2Si, $CaSi$ and $CaSi_2$ for ab initio modeling of their optical properties. Firstly, full structural optimization of these silicides both in the bulk and thin film forms was carried out by the first-principles total energy projector-augmented wave method (VASP code).[55–58] within the GGA of Perdue–Burk–Ernzerhoff.[59] The calculations were performed by implementing the energy cutoff of 320 eV. The number of k-points for the Brillouin zone integration was sufficient to assure the total energy convergence was better than 1 meV atom^{-1}. Structural optimization was stopped when the forces acting on the atoms were less than 0.01 eV Å^{-1}. Then calculations of optical functions of the Ca silicides were carried out using the full-potential linearized augmented plane wave method (WIEN2k package)[66] within the GGA of Perdue–Burk–Ernzerhoff.[59] The structural parameters of the Ca silicides fully optimized by the projector-augmented wave method have been taken into consideration. The absorption coefficient and reflectivity have been estimated at a dense mesh of at least 700 k-points in the irreducible part of the corresponding Brillouin zone.

3. Results

### 3.1. Peculiarities of the crystal structure of the Ca silicide films and their matching with silicon

Our investigation on the growth of single-phase Ca_2Si films on silicon were primarily devoted to the study of their crystal structure by the transmission electron microscopy (TEM) method on cross-sections, since such data were absent in our previous work.[21,25] Figure 1 shows cross-sectional images of two samples with Ca_2Si films grown by MBE at a temperature of 250 °C using the sacrificial-template technique. The films were thinned for TEM on cross-sections approximately 8 months after they were unloaded, sent and stored in air, so both films have a clearly visible oxide layer in the amorphous state with a thickness of 20–25 nm, but then the columnar structure of Ca_2Si grains perpendicular to the silicon substrate is clearly visible [Figs. 1(a) and 1(b)]. The high-resolution TEM (HRTEM) images for both samples [Figs. 1(c) and (d)] confirmed the orthorhombic structure (the 62 space group) of Ca_2Si with $Ca_2Si(100)//Si(111)$ and $Ca_2Si[010]//Si[\bar{1}12]$ epitaxial relationships. According to the energy dispersive spectroscopy (EDX) data [Figs. 1(e) and 1(f)] in both

samples, in addition to a thick oxide layer on the surface, an increased oxygen concentration is observed along the depth, which may be due to the high oxidizability of the obtained cross-sections after their ion thinning and before viewing in TEM. The second feature in both samples is the presence of a thin layer enriched with magnesium at the interface with the silicon substrate.

Let us consider the formation and structure of a single-phase CaSi film formed on Si(111) in sample *D*. Figure 2(a) shows the film morphology according to AFM data. After the formation of the Ca_2Si template, the sample was subjected to calcium combined deposition, first at a temperature of 300 °C and then at 400 °C. After that, it was covered with a thin amorphous layer of silicon about 5 nm thick (Table I), which oxidized during storage. After the growth procedure, a continuous film of calcium silicide was formed [Fig. 2(a)] with an RMS roughness of 4.0 nm and no signs of grain crystallization. However, according to XRD spectra (not shown) and TEM data on the cross-section [Fig. 2(b)]; the film consists of individual vertically grown grains. The study of the elemental composition of the grown film was carried out by EDX. To avoid the contribution from the Si substrate and from the Si and Ca oxides that are on the film surface, a specific region located far from the film—Si substrate interface and from the film surface was chosen for the EDX analysis. This area is circled (EDX-area) in the TEM image shown in Fig. 2(b). As follows from the EDX results [Table in Fig. 2(b)], the atomic concentrations of Ca and Si atoms are very close, so the grown film has the CaSi composition. The HRTEM image [Fig. 2(c)] shows that the film has grown epitaxially on the Si(111) substrate with visible twin lamellae [top right and center in Fig. 2(c)]. To determine the epitaxial relationships, two regions of the film were selected, corresponding to two different CaSi grains, and the region of the Si substrate far from the CaSi film—Si substrate interface. Fast Fourier transform (FFT) images were acquired from these regions and shown in Figs. 2(d), (e), which were typical of the other regions of the film. Grains of different Ca silicides were not observed in the film.

The FFT image for the first type of CaSi grains [region 1 in Fig. 2(c)] is shown in Fig. 2(d). It suggests the following epitaxial relationship: $CaSi[001]||Si[\bar{1}10]$ and $CaSi(220)||Si(111)$. From the FFT image for the first grain, the interplanar distances of 0.2279 and 0.5396 nm for the CaSi(200) and CaSi(020) planes were respectively obtained resulting in the $a = 0.4558$ nm and $b = 1.0793$ nm lattice constants. It turned out that a was slightly compressed by 0.04% in the $CaSi[100]$ direction and b was stretched by 0.57% in the $CaSi[010]$ direction. For the second type of CaSi grains [region 2 in Fig. 2(c)], the FFT image shown in Fig. 2(e) indicates the following epitaxial relationship: $CaSi[00\bar{1}]||Si[\bar{1}10]$ and $CaSi(220)||Si(111)$, where interplanar distances of 0.2241 and 0.5528 nm have been obtained for the CaSi(200) and CaSi(020) planes. In this case $a = 0.4483$ nm is compressed by 1.68% in the $CaSi[100]$ direction and $b = 1.1057$ nm is stretched by 3.03% in the $CaSi[010]$ direction. We found CaSi grains of the second type to dominate indicating that the most preferable epitaxial relationship is $CaSi[00\bar{1}]||Si[\bar{1}10]$ and $CaSi(220)||Si(111)$.

The calculated lattice parameters of CaSi and observed epitaxial relationship to Si(111) allows for constructing a
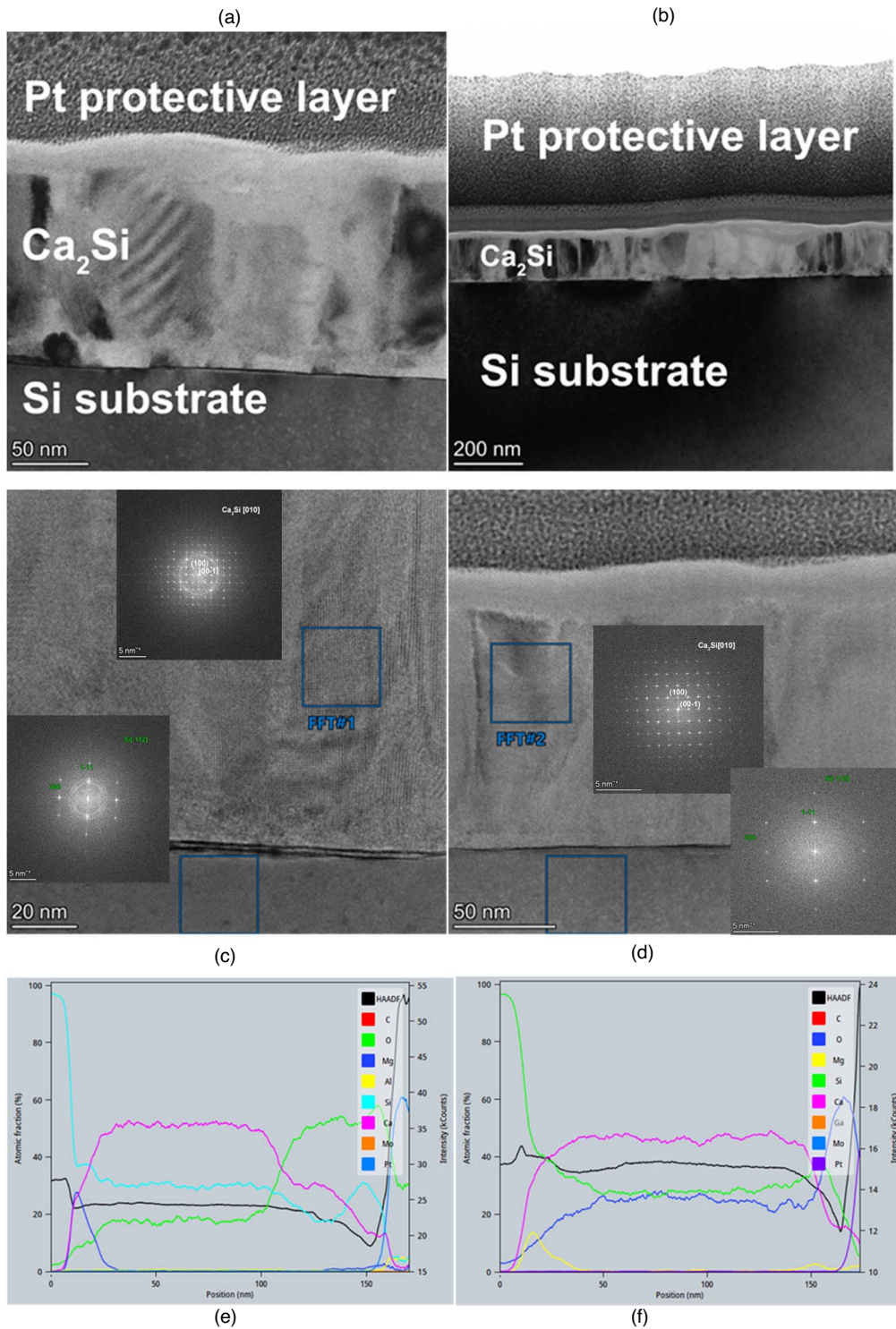
Fig. 1. (Color online) (a) and (b) TEM; (c) and (d) HRTEM; (e) images and distribution of elements in the film and substrate according to EDX, and (f) spectroscopy data in samples *A* and *B* with Ca₂Si films on Si(111), respectively. Insets in (c) and (d) are FFT patterns from films highlighted in blue squares [FFT-1 (sample *A*) and FFT-2 (sample *B*)] and from a silicon substrate.
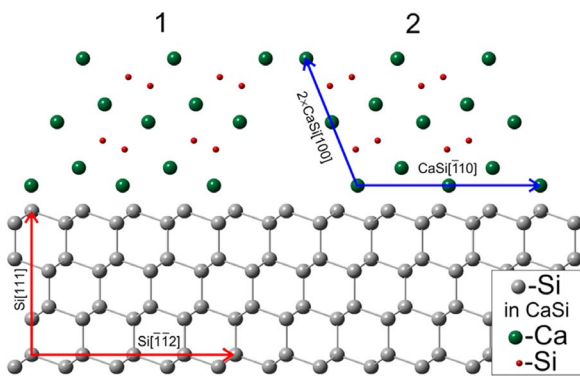
model of matching of lattices of CaSi grains of both types with the Si substrate (Fig. 3). For the second type grain on the CaSi(220) plane, the base lattice vectors are the orthogonal CaSi[00$\bar{1}$] and CaSi[$\bar{1}$10] vectors with CaSi[00$\bar{1}$]||Si[$\bar{1}$10] and CaSi[$\bar{1}$10]||Si[$\bar{1}$$\bar{1}$2]. At the same time, for the CaSi lattice parameters $a = 0.4483$ nm, $b = 1.1057$ nm, and $c = 0.389$ nm, the lattice mismatch in the Si[$\bar{1}$10] direction

is small (1.31%), while in the Si[$\bar{1}$$\bar{1}$2] direction, a noticeable mismatch of -10.3% is observed. For the first type grain on the CaSi(220) plane, the base lattice vectors are the orthogonal CaSi[001] and CaSi[1 $\bar{1}$0] vectors with CaSi[001]||Si[$\bar{1}$10] and CaSi[1$\bar{1}$0]||Si[$\bar{1}$$\bar{1}$2]. If we compare these relationships of both types of grains, it turns out that rotation of the CaSi lattice by 180° of the CaSi(220) plane is necessary for

(a)

(b)

(c)   (d)   (e)
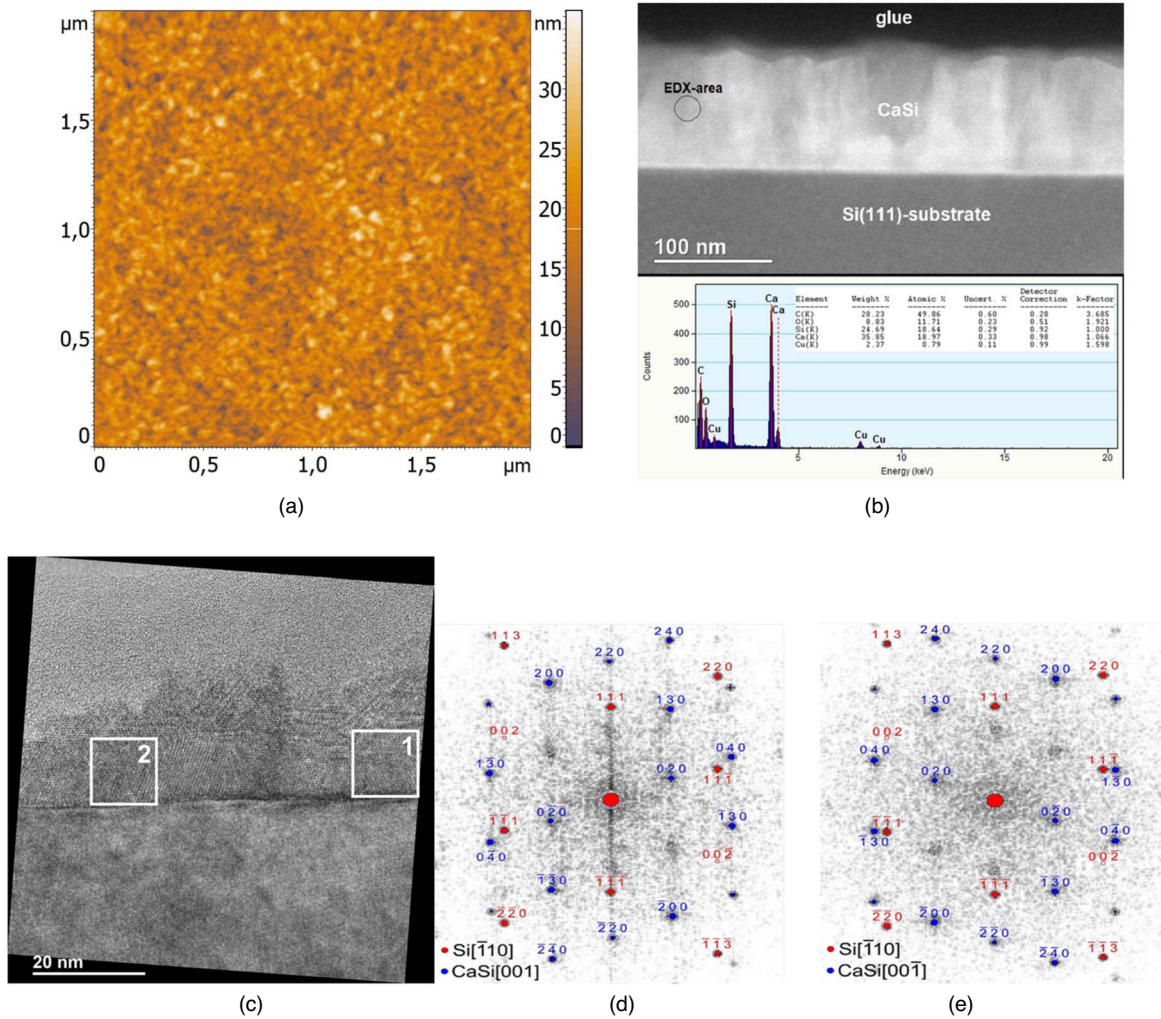
Fig. 2. (Color online) Sample *D*: (a) AFM morphology of the grown film; (b) TEM image of the cross- section and EDX data; (c) HRTEM image of a sample fragment selected near the interface in cross-section in the Si[1$\bar{1}$0] direction. The square white frames mark 2 areas in which the FFT images for the film were obtained; film FFT images were taken in region 1 (d) and region 2 (e).


Fig. 3. (Color online) Models of lattices of CaSi grains of the first (1) and second (2) types on the Si(111) surface constructed perpendicular to the Si[1$\bar{1}$0] direction. Lattice constants for CaSi: $a = 0.4483$ nm (-1.68%), $b = 1.1057$ nm (3.03%) and $c = 0.389$ nm (0%), for Si: $a = 0.543$ nm.

the first type (Fig. 3) to fulfill the CaSi[001]||Si[$\bar{1}$10] and CaSi[1$\bar{1}$0]||Si[$\bar{1}$ $\bar{1}$2]. The difference between the models for CaSi grains is most clearly seen when they are built perpendicular to the Si[1 $\bar{1}$0] direction. In this perspective,

the model for the CaSi grain of the first type is a mirror image of the model for the CaSi grain of the second type.

Let us consider the morphology and structure of a single-phase sample of calcium disilicide (CaSi$_2$) in sample *G* (Fig. 4), which was formed on the Si(001) surface during the co-deposition of Ca and Si atoms with a low rate ratio at the substrate temperature $T = 500$ °C (Table I). The HRTEM image for sample G [Fig. 4(a)] shows that the Ca silicide film has grown epitaxially on the Si(001) substrate. Due to the fact that the Ca deposition rate was low and the substrate temperature was high, the accommodation coefficient of calcium to silicon was low leading to a thickness of no more than 15 nm [Fig. 4(a)]. This correlates with the morphological data on the AFM image [Fig. 4(b)] and the low RMS film roughness (1.9 nm). To determine the epitaxial relationships, two regions of the film were selected with two different grains of Ca silicide in addition to a region of the Si substrate being far from the Ca film–Si substrate interface. FFT images were acquired from these regions [Figs. 4(c), 4(d)]. Note, the obtained FFT images are also observed in the other regions of the film and correspond to two types of
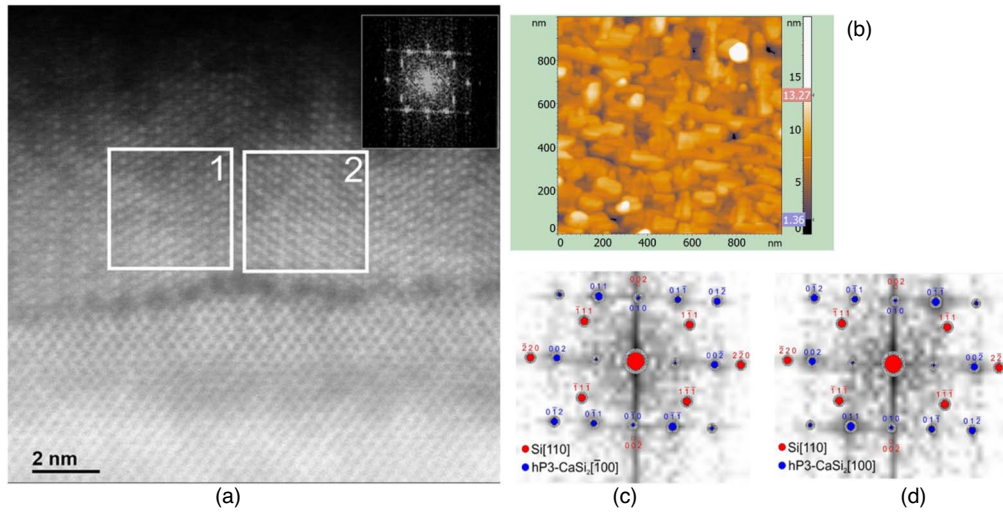
Fig. 4. (Color online) (a) HRTEM image of a fragment of sample G obtained in cross-section in the Si[110] direction. The square white frames mark two areas in which FFT images were obtained for the film. (b) AFM image of the film in sample *G*; (c) and (d)—FFT of the image from areas (1) and (2), respectively.

calcium disilicide grains with the hP3-CaSi$_2$ structure, which is discovered for the first time. Grains of other Ca silicides are not detected in the film.

The FFT image for the first type of the hP3-CaSi$_2$ grain with hP3-CaSi$_2$[$\bar{1}$00]||Si[110] and hP3-CaSi$_2$(010)||Si(002) epitaxial relationships is shown in Fig. 4(c). The corresponding interplanar distances for the hP3-CaSi$_2$(010) and hP3-CaSi$_2$(002) planes are 0.3284 nm and 0.256 nm, respectively, pointing out shrank lattice parameters $a = 0.3793$ nm (-1.49%) along hP3-CaSi$_2$[100], hP3-CaSi$_2$[010] directions and $c = 0.5121$ nm (-1.53%) along the hP3-CaSi$_2$[001] direction. For the second type of CaSi grain, the FFT image is shown in Fig. 4(d) and the hP3-CaSi$_2$[100]||Si[110] and hP3-CaSi$_2$(010)||Si(002) epitaxial relationships can be drawn. From this FFT image, interplanar distances of 0.3303 and 0.2505 nm were obtained for the hP3-CaSi$_2$(010) and hP3-CaSi$_2$(002) planes with the shrank lattice parameters ($a = 0.3814$ nm (-0.92%) and $c = 0.5009$ nm (-3.67%)). The lattice of such a grain is compressed by 0.92% in the hP3-CaSi$_2$[100] and hP3-CaSi$_2$[010] directions, and compressed by 3.67% in the hP3-CaSi$_2$[001] direction. The number of hP3-CaSi$_2$ grains of the different types in the film is approximately the same. Therefore, we assumed that the probability of the formation of grains of the first and second types is approximately equal.

Fig. 5. (Color online) Models of hP3-CaSi$_2$ grain lattices of the first (1) and second (2) types on the Si(001) surface constructed perpendicular to the Si[110] direction.

On the basis of the calculated lattice parameters and epitaxial relationships, it is possible to construct a model of matching of the hP3-CaSi$_2$ grain lattices with the Si(001) surface for grains of the second type (Fig. 5). On the hP3-CaSi$_2$(010) plane, the base vectors of the lattice are the orthogonal hP3-CaSi$_2$[100] and hP3-CaSi$_2$[001] vectors with the following relationships: hP3-CaSi$_2$[100]||Si[110] and hP3-CaSi$_2$[001]||Si[1$\bar{1}$0]. At the same time, for the hP3-CaSi$_2$ lattice parameters $a = 0.3814$ nm (-0.92%) and $c = 0.5009$ nm (-3.67%), the lattice mismatch in the Si[110] direction is small (-0.65%), while in the Si[1$\bar{1}$0] direction the mismatch is noticeably larger (-2.15%). For the first type grain on the hP3-CaSi$_2$(010) plane, the base vectors of the lattice are the orthogonal hP3-CaSi$_2$[$\bar{1}$00] and hP3-CaSi$_2$[00$\bar{1}$] vectors with the hP3-CaSi$_2$[$\bar{1}$00]||Si[110] and hP3-CaSi$_2$[00$\bar{1}$]||Si[1$\bar{1}$0] relationships. This corresponds to the rotation of the hP3-CaSi$_2$ lattice in the hP3-CaSi$_2$(010) plane by 180°, as seen in Fig. 5, and to a mirror reflection of the hP3-CaSi$_2$ grain model of the second type with respect to the first type.

To grow a thick film of calcium disilicide on a Si(001) substrate, the MBE method was used at the substrate temperature $T = 680$ °C with a sharp calcium supersaturation ($v_{Ca}: v_{Si} = 26.3$) and a deposition time of 100 min (Table I, sample H). According to AFM data [Fig. 6(a)], the film consists of mutually perpendicular grains with sizes from 0.5 to 5 μm. The surface of the grains is smooth with an RMS roughness of 2.3 nm. There are also small and deep dips between the grains caused by the fact that the interface during growth is highly inhomogeneous, which is clearly seen in the TEM image [Fig. 6(b)]. The average film thickness is 382 nm. The film is homogeneous and consists of large grains. The silicide film–Si substrate interface is sharp, but uneven, which is associated with the active participation of silicon atoms from the substrate during silicide formation. The HRTEM image [Fig. 6(c)] shows that the film has grown epitaxially on Si(001) with the presence of twin lamellae [on the right in Fig. 6(c)]. To determine the epitaxial relationships, two regions of the film and one region of the silicon substrate were chosen for FFT images analysis [see Figs. 6(d), 6(e)]. The grown film is CaSi$_2$ with the
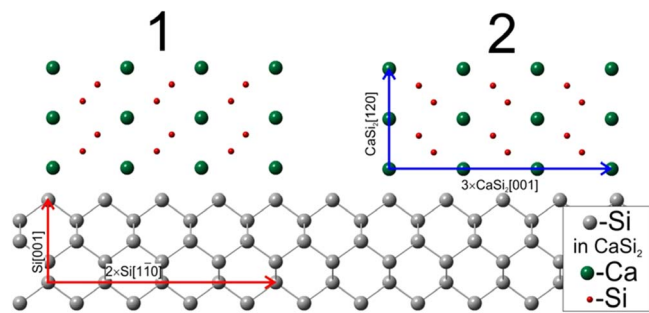
(a)   (b)

(c)   (d)   (e)
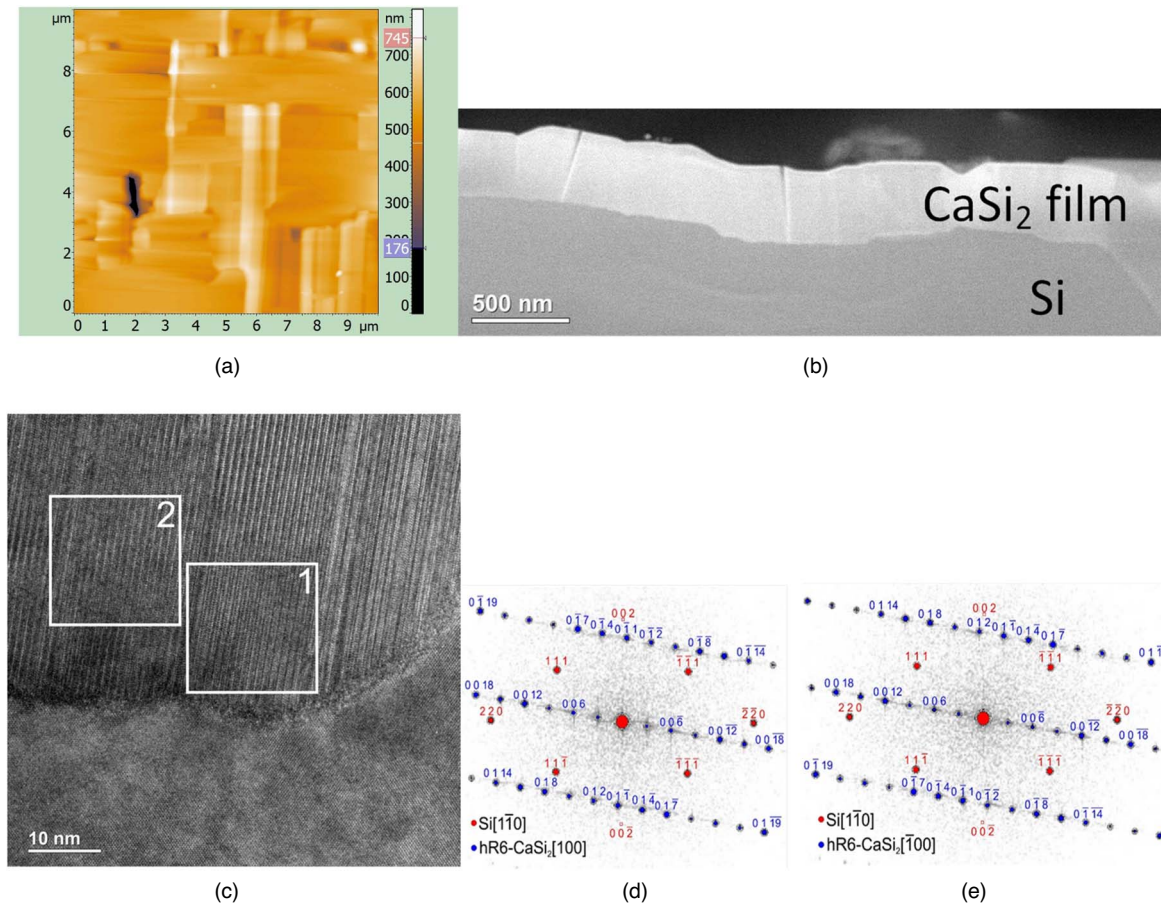
Fig. 6. (Color online) Sample *H*: (a) AFM image of the film surface; (b) HRTEM image of the sample taken in cross-section in the Si[1$\bar{1}$0] direction. The square white frames mark 2 areas in which the FFT images for the film were obtained; (d) and (e)—FFT of the image from areas (1) and (2), respectively. The position of reflections for the Si substrate (red circles) was obtained from the FFT image for the Si substrate region in the HRTEM image (c).

hR6-CaSi$_2$ structure.[37] Grains of other Ca silicides are not observed n the film. For the hR6-CaSi$_2$ grain in the region 1, the hR6-CaSi$_2$[100]||Si[1$\bar{1}$0] and hR6-CaSi$_2$(01$\bar{1}$)||Si(002) epitaxial relationships have been found. Note that the hR6-CaSi$_2$(01$\bar{1}$) and Si(002) planes are not strictly parallel displaying the misorientation angle of 3.2°. From the FFT image, interplanar spacings of 0.3313 nm and 0.51 nm were obtained for the hR6-CaSi$_2$(01$\bar{1}$)and hR6-CaSi$_2$(006) planes, respectively, with the lattice parameters a = 0.3848 nm (−0.31%) and c = 3.0604 nm (0.01%). It is turned out that the lattice is compressed by 0.31% in the hR6-CaSi$_2$[100] and hR6-CaSi$_2$[010] directions and practically unchanged (stretching is only 0.01%) in the hR6-CaSi$_2$[001] direction. The model of matching of such a lattice with the Si(001)

plane is shown in Fig. 7 displaying a good agreement: the lattice mismatch is 0.22% for the Si[1$\bar{1}$0] and Si[$\bar{1}$10] directions. The base lattice vectors: doubled hR6-CaSi$_2$[100] and hR6-CaSi$_2$[122] differ by 8 times.

For another hR6-CaSi$_2$ grain, which is located nearby [region 2 in Fig. 6(c)], the following epitaxial relationships are detected: hR6-CaSi$_2$[100]||Si[1$\bar{1}$0] and hR6-CaSi$_2$(012)||Si(002). The hR6-CaSi$_2$(012) and Si(002) planes are also not strictly parallel with the misorientation angle of 3.2°. For the hR6-CaSi$_2$(012) and hR6-CaSi$_2$(006) planes, the interplanar distances are 0.3252 and 0.5165 nm that corresponds to the a = 0.3841 nm (−0.49%) and c = 3.0992 nm (1.28%) lattice parameters which are compressed by 0.49% in the hR6-CaSi$_2$[100] and
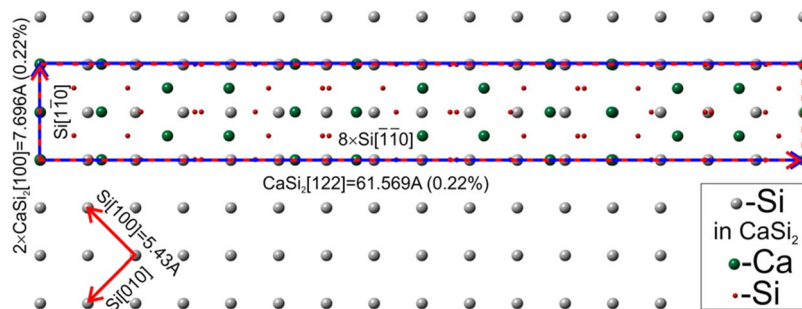
Fig. 7. (Color online) Model of the hR6-CaSi$_2$ lattice on the Si(001) surface constructed for the epitaxial relationships hR6-CaSi$_2$[100]||Si[1$\bar{1}$0] and hR6-CaSi$_2$(01$\bar{1}$)||Si(002). The red dotted lines indicate the directions of the axes of the hR6-CaSi$_2$ (01$\bar{1}$) superlattice and the superlattice cell, and the blue line marks the area of the silicon supercell.
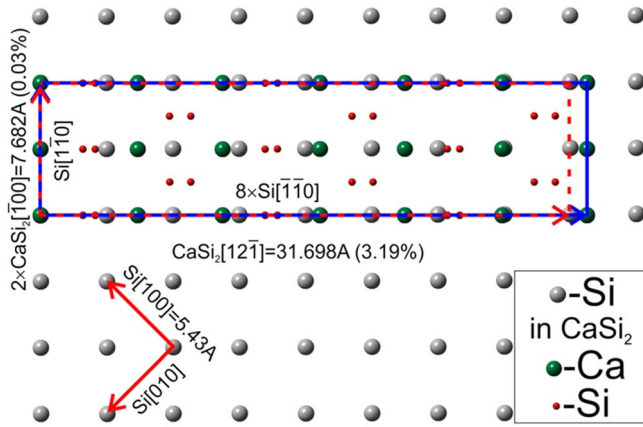
Fig. 8. (Color online) Model of the hR6-CaSi$_2$ lattice on the Si(001) surface constructed for the epitaxial relationships hR6-CaSi$_2$[$\bar{1}$00]||Si[1$\bar{1}$0] and hR6-CaSi$_2$(012)||Si(002). The red dotted lines indicate the directions of the axes of the hR6-CaSi$_2$ (012) superlattice and the superlattice cell, and the blue line marks the area of the silicon supercell.

hR6-CaSi$_2$[010] directions and stretched by 1.28% in the hR6-CaSi$_2$[001] direction. The corresponding model of matching of hR6-CaSi$_2$ with the Si(001) plane is shown in Fig. 8 and characterized by the lattice mismatches of 0.03% and 3.19% in the Si[1$\bar{1}$0] and Si[$\bar{1}\bar{1}$0] directions, respectively. Since the base vectors of the lattice (doubled hR6-CaSi$_2$[100] and hR6-CaSi$_2$[12$\bar{1}$]) differ by a factor of 4, its area is approximately 2 times smaller than that of the model shown in Fig. 7.

The growth of a single-phase film of CaSi$_2$ on an atomically clean Si(111)7 × 7 surface was also carried out by the MBE method at a temperature of 500 °C with a Ca to Si deposition rate ratio of 7.7. On the surface of the formed film in sample *J*, thin crystals of small height and sizes of 50–200 nm are observed (Fig. 9(a)), but the film has a low RMS roughness (1.6 nm). The XRD data [Fig. 9(b)] shows thin and intense peaks of the hR6-CaSi$_2$ crystalline phase with a series of planes: (006), (0012), (0015), (0018), (0030), which corresponds to the epitaxial ordering of hR6-CaSi$_2$(006)//Si(111) without grains with other orientations.

It is not straightforward to fabricate non-single-phase silicide films on a silicon or sapphire substrate containing nanocrystals of silicide phases, which have not previously been grown in the form of thin films such as Ca$_5$Si$_3$ and Ca$_{14}$Si$_{19}$. To form Ca$_5$Si$_3$, we propose to form CaSi by MBE first with an average calcium supersaturation (v_{Ca}: $v_{Si} = 3.2$) at a temperature of 400 °C, and then gradually increase the Ca concentration sequentially at three stages of Ca reactive deposition at 490 °C, 600 °C and 700 °C (Table I, sample *L*). Following this procedure the formation of a textured silicide film [Fig. 10(a)] consisting of crystals 100–150 nm wide and 0.3–0.7 μm long occurred. The obtained film had a small relief with an RMS roughness of 2.3 nm. According to XRD data, we have detected two types of nanocrystals bounded by the Ca$_5$Si$_3$(004) and CaSi(021) planes [Fig. 10(b)], which are parallel to the substrate plane: CaSi(021)||Si(001) and Ca$_5$Si$_3$(001)||Si(001). The Ca$_5$Si$_3$(001) plane is formed by two mutually perpendicular vectors: Ca$_5$Si$_3$[1$\bar{1}$0] =1.0818 nm and Ca$_5$Si$_3$[110] = 1.0818 nm. The half-width of the XRD peak from CaSi(021) was significant indicating the small sizes of the nanocrystals. Contrary, the peak from the Ca$_5$Si$_3$ phase was very narrow, typical of large crystal sizes that correlate well with the AFM data [Fig. 10(a)].

We have also used a sapphire substrate to grow Ca$_5$Si$_3$ by MBE at 470 °C and Ca to Si deposition rate ratio of 4.0. There were found three types of nanocrystals [Fig. 10(d)] including hR6-CaSi$_2$(110) (main contribution), CaSi(006) (intermediate contribution) and Ca$_5$Si$_3$(123) nanocrystals (minimum contribution). Consequently, a higher substrate temperature (700 °C) with an additional flow of Ca atoms led to a more significant growth of Ca$_5$Si$_3$ crystals and their crystallization. Thus, the lower temperatures during the MBE growth without an additional flow of Ca atoms (sample *D*) do not promote the appearance of the Ca$_5$Si$_3$ phase.

The formation of the Ca$_{14}$Si$_{19}$ phase was carried out on a Si(111) substrate by a combination of two growth methods: first, by RDE at 500 °C and at a low deposition rate of Ca atoms to form a template, and then by MBE at a ratio of Ca to Si deposition rates of 2:1 and a substrate temperature of 500 °C (Table I, sample *N*). The grown film consisted of crystals intergrown at angles of 60° and 120° [Fig. 10(b)] with sizes from 100 to 500 nm. An analysis of the XRD data
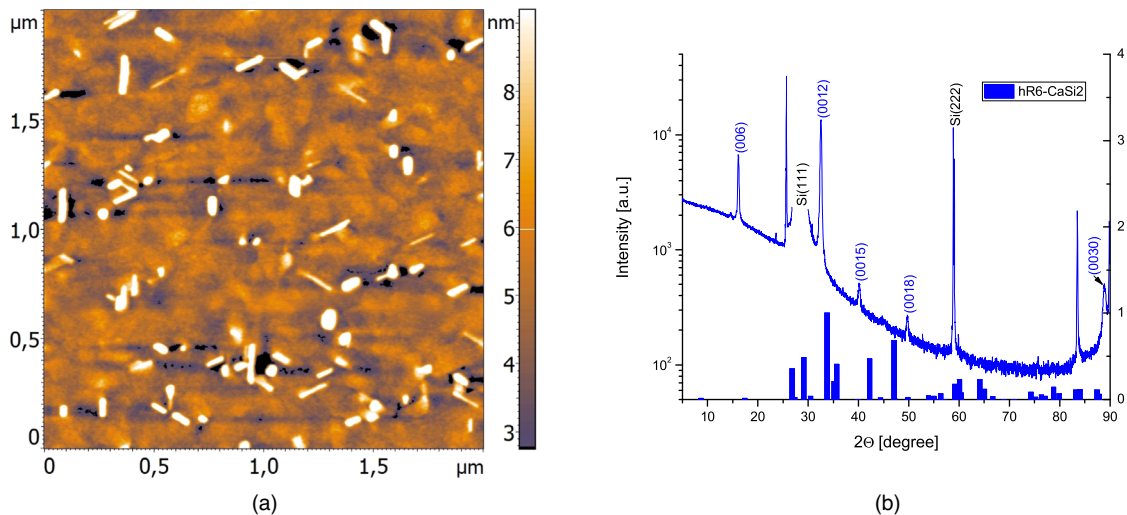
Fig. 9. (Color online) (a) AFM image of a CaSi$_2$ film on a Si(111) substrate and (b) XRD spectrum in sample *J*.
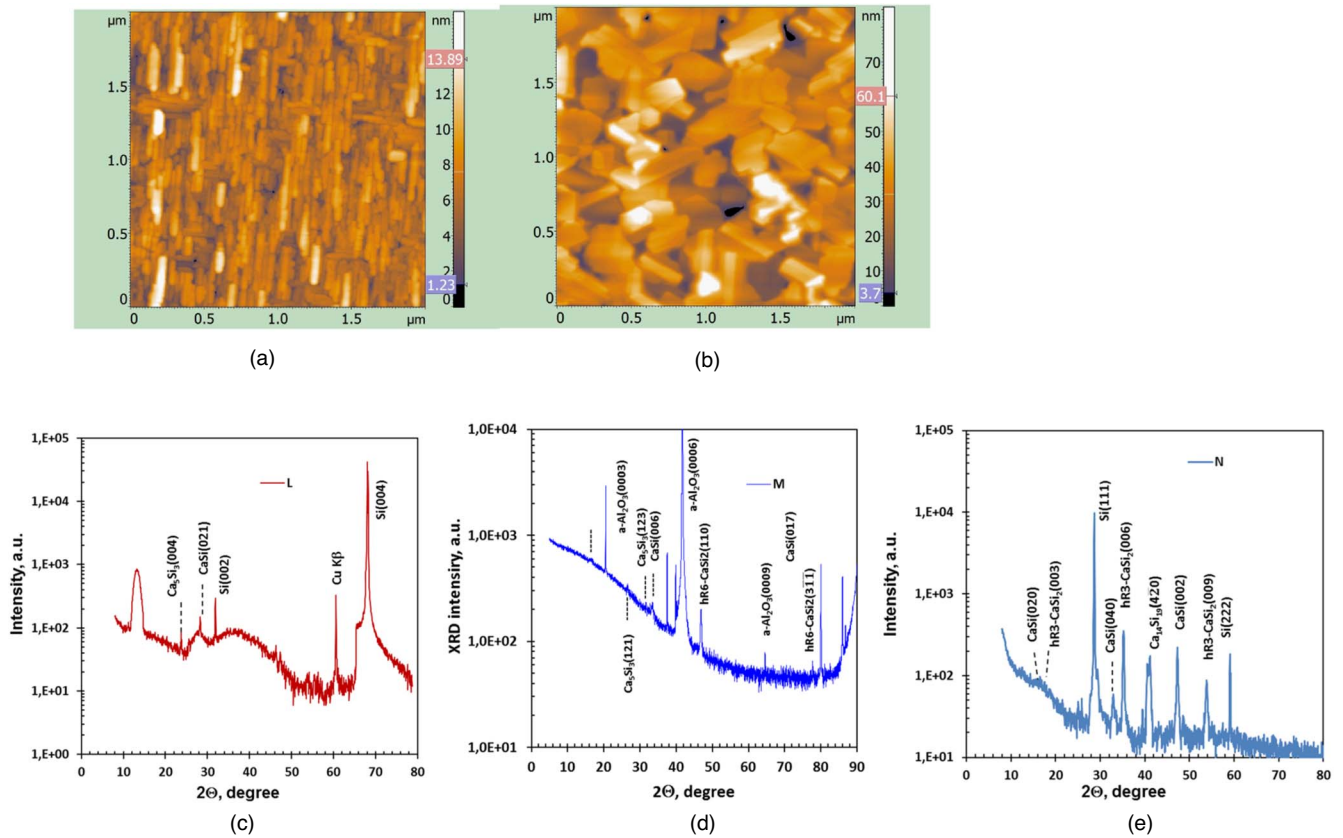
Fig. 10. (Color online) AFM images: (a) for film in sample *L*; (b) for a film in sample *M*. XRD spectra for samples with films containing silicide phases: Ca_5Si_3 (samples *L*, *M*) (c), (d) and $Ca_{14}Si_{19}$ sample *N*) (e).

[Fig. 10(e)] showed that the main contribution comes from hR3-CaSi₂(003) and CaSi(002) crystals with approximately equal proportions in addition to a smaller contribution of $Ca_{14}Si_{19}(4\bar{2}0)$, all parallel to the Si(111) plane. Despite the smaller contribution, we are interested in the matching of the $Ca_{14}Si_{19}$ phase (peak $2\Theta = 41.16°$) with silicon, which has not been observed before in our experiments and providing the model of this matching. The peak observed in the XRD spectrum corresponds to the $Ca_{14}Si_{19}(4\bar{2}0)$ plane. There are two perpendicular vectors on this plane: $Ca_{14}Si_{19}[120]$ and $Ca_{14}Si_{19}[001]$. $Ca_{14}Si_{19}$ has a hexagonal structure (R-3m) and the following lattice parameters: $a = 0.86714$ nm, $c = 6.8569$ nm.[49] For such lattice parameters, the length of the $Ca_{14}Si_{19}[120]$ vector is 1.5019 nm, which is 2.22% less than the length of two $Si[1\bar{1}0]$ vectors. Whereas the length of the $Ca_{14}Si_{19}[001]$ vector is 6.8569 nm, which is 3.11% more

than the length of 5 $Si[11\bar{2}]$ vectors. Therefore, the following epitaxial relations hold on the Si(111) surface: $Ca_{14}Si_{19}[120]||Si[1\bar{1}0]$ and $Ca_{14}Si_{19}[001]||Si[11\bar{2}]$.

The model to form a commensurate match of the $Ca_{14}Si_{19}$ grain on the Si(111) surface is shown in Fig. 11. We also used the $Ca_{14}Si_{19}$ bulk lattice parameters ($a = 0.86714$ nm, $c = 6.8569$ nm,[49]) as well as epitaxial relationships: $Ca_{14}Si_{19}(2\bar{1}0)||Si(111)$, $Ca_{14}Si_{19}[120]||Si[1\bar{1}0]$ and $Ca_{14}Si_{19}[001]||Si[11\bar{2}]$. The area of the $Ca_{14}Si_{19}$ cell bounded by blue arrows and lines in Fig. 11 is equal to 10.298 nm². It is 0.82% larger than the cell area bounded by vectors $Si[2\bar{2}0]$ and $Si[55\bar{1}0]$ (10.214 nm²).

3.2. Optical functions and transparency of Ca silicide films

Our next step is to carefully examine the optical functions of single-phase Ca_2Si, $CaSi$, and $CaSi_2$ films obtained by
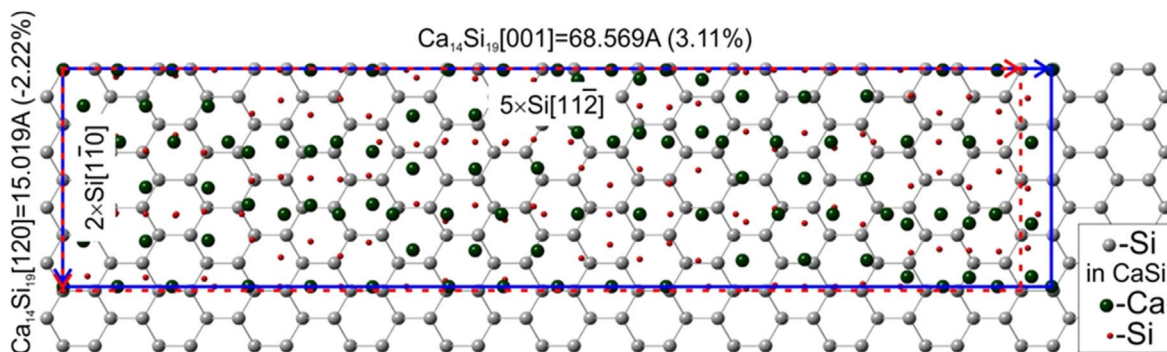

Fig. 11. (Color online) Model of a $Ca_{14}Si_{19}$ grain cell on a Si(111) surface. The red dotted lines indicate the directions of the axes of the $Ca_{14}Si_{19}(2\bar{1}0)$ superlattice and the superlattice cell, and the blue line marks the area of the silicon supercell.
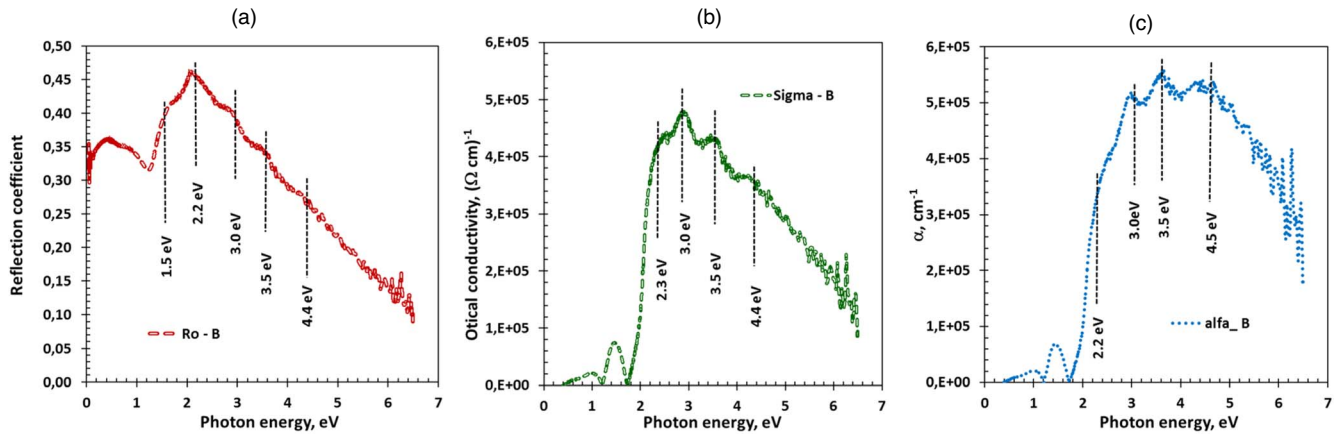
Fig. 12. (Color online) Optical spectral functions of the Ca$_2$Si film in the sample *B*: (a) reflection coefficient; (b) absorption coefficient and (c) optical conductivity.

experimental measurements and theoretical calculations. Figure 12 shows the reflection spectrum, as well as the main optical functions for the Ca$_2$Si film in sample *B*, calculated from the reflection spectrum using the Kramers–Kronig integral relations.[26] The true reflection spectrum for the Ca$_2$Si film in the photon energy range (0.04–1.2 eV) was calculated from the two-layer model by subtracting the contribution from the reflection from the silicon substrate and taking into account its absorption coefficient as well as multiple passages of radiation through the film–substrate system.[54] The total reflectance spectrum is in good agreement with the published data for the Ca$_2$Si epitaxial film.[17] The calculated absorption coefficient [Fig. 12(b)] shows the onset of stable absorption in the film at energies above 1.7 eV and some absorption bands in the photon energy range of 0.4–1.7 eV, which may be due to absorption caused by a high defect density.

A decrease in the measured reflectance due to irretrievable losses in the film relief leads to a decrease in the refractive index and distortions in the extinction coefficient, which also leads to losses in the absorption coefficient. These losses and defect states completely mask the region of the fundamental transition in the Ca$_2$Si film in our calculations by the Kramers–Kronig method,[26] in comparison with calculations from the transmission and reflection spectra in the framework of the two-layer model,[54] both on silicon and on sapphire.[21,27] The optical conductivity spectrum [Fig. 12(c)] resembles in shape the spectrum of the absorption coefficient and indicates the decisive role in the optical conductivity of interband transitions in Ca$_2$Si above 2 eV. A comparison of the optical functions of the Ca$_2$Si film with the data of theoretical calculations for bulk Ca$_2$Si and its films of different thicknesses (Fig. 13) showed a good agreement in the shape of the reflection spectra [Fig. 12(a)], but not in the position of the fundamental absorption edge and not in the values of the absorption coefficient at photon energies from 1.2 to 1.6 eV. The experimental values of the absorption coefficient at 1.4 eV are 3–4 times lower than the calculated values. Since the experimental absorption coefficient was evaluated from the experimental reflection spectra, the underestimation of the absorption coefficient in the region of the main transitions and its "blue" shift to the region of stronger interband transitions [Fig. 12(b)] are associated with
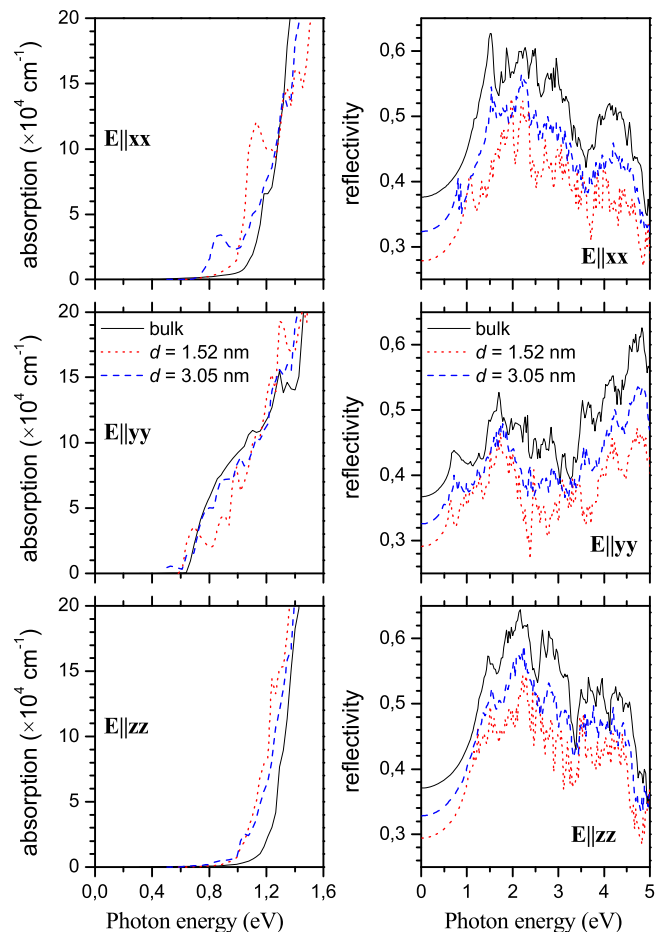
Fig. 13. (Color online) Dependence of optical absorption and reflection coefficients on photon energy for Ca$_2$Si(100) thin films in comparison with bulk material for different light polarizations (*E||xx*, *E||yy*, and *E||zz*).

irretrievable losses in the relief of the Ca$_2$Si film. The data of theoretical calculations for bulk Ca$_2$Si and its thin films (Fig. 13) showed a slight decrease in the reflection coefficient without changing their spectral composition at different light polarizations, as well as small shifts along the fundamental absorption edge. That is, despite the small thicknesses of the Ca$_2$Si films (1.52 and 3.05 nm), no noticeable changes in the density of states were observed compared to bulk Ca$_2$Si.

Samples *D* and *E* are examples of single-phase CaSi films (Table I). Sample *D* was fabricated by MBE at *T* = 400 °C
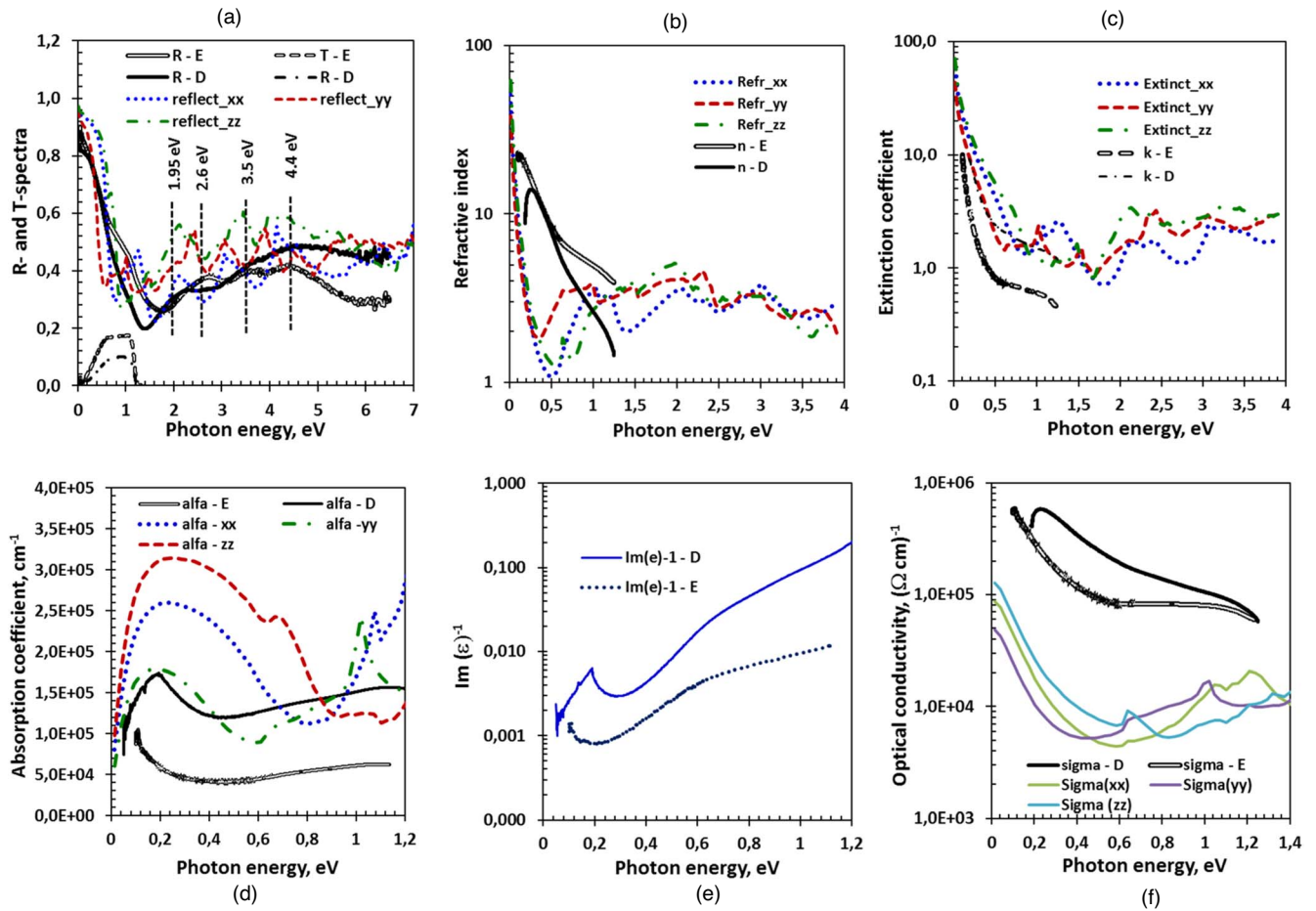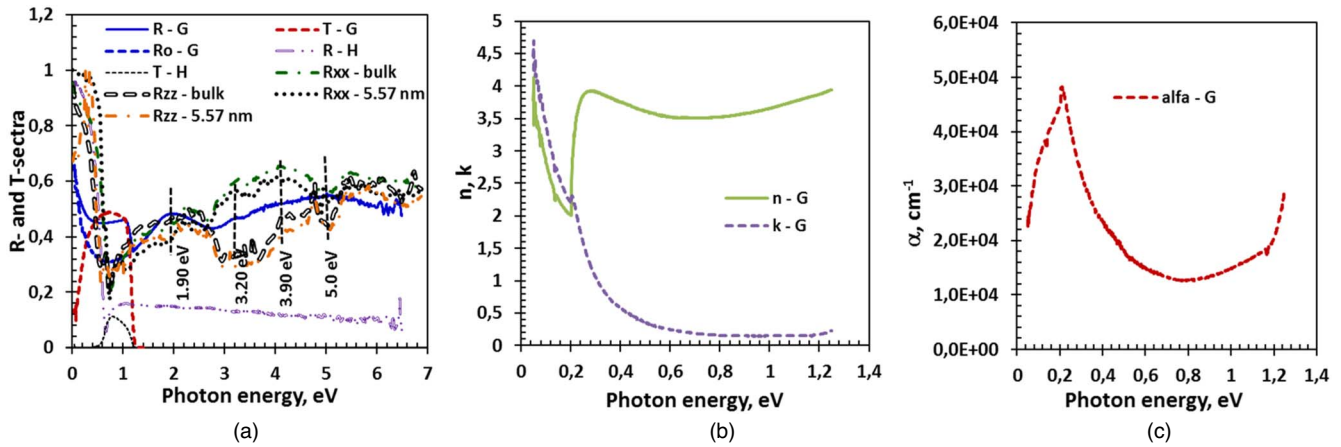
Fig. 14. (Color online) Experimental spectra of optical functions of CaSi films in samples D and E and theoretical spectra for bulk CaSi: (a) reflection coefficients; (b) refractive indexes; (c) extinction coefficients; (d) absorption coefficients; (e) dielectric loss functions and (f) optical conductivity. Ab initio calculations of the reflection spectra were carried out for different light polarizations ($E||xx$, $E||yy$, and $E||zz$).

through the formation of a sacrificial Mg_2Si layer and a Ca_2Si template, while sample E was obtained by RDE at $T = 475$ °C.[23] Since the samples showed different epitaxial orientations of CaSi grains, it is interesting to compare the experimental data and results of first-principles calculations on optical function. Figure 14(a) shows the experimental reflection spectra for CaSi films in samples D and E and the theoretical spectra for bulk CaSi. In both experimental reflection spectra, a pronounced plasma minimum is observed at photon energies of 1.4 and 1.8 eV and a reflection maximum with a value of 0.85–0.9 at photon energy of about 0.04 eV.[26] At energies above 1.95 eV, local maxima are seen with small shifts in energy, which can be attributed to reflection from CaSi grains with different orientations in the studied films. The grown films show different transmissions in the photon energy range of 0.1–1.2 eV, which is associated with different thicknesses of the grown films (Table I). The calculations of the reflection spectra from the band energy structure for a bulk CaSi single crystal at different light polarizations [Fig. 14(a)] showed a good agreement, both in the shape of the spectra and in their amplitude, but some discrepancy in the position of the plasma minimum, as well as in the maxima and minima compared to the experimental spectra was evident. Calculations of the spectra of the refractive index [Fig. 14(b)] and the extinction coefficient [Fig. 14(c)] on the basis of the experimental spectra in the framework of the two-layer model gave some

discrepancy with the theoretical spectra in the region of photon energies below 1.0 eV for different light polarizations for the refractive index and qualitative agreement for the extinction coefficient [Fig. 14(c)].[54] The differences found are due to the fact that the films are polycrystalline and contain a certain number of defects, which leads to the appearance of additional defect states in the gap. The CaSi film in sample D seems to have more of these defects that leads to a noticeable increase in the absorption coefficient in the photon energy range of 0.1–1.2 eV [Fig. 14(d)] compared to the film in sample E grown at a higher temperature. In a CaSi single crystal, the absorption coefficient is higher at photon energies from 0.2 to 0.8 eV, which suggests a larger number of free carriers, which determine the contribution to plasma reflection at low photon energies. The dielectric loss function for the grown films also shows its decrease and then increase as the photon energy falls below 0.3 eV [Fig. 14(e)]. The latter is related to the contribution of absorption at defects, which, however, do not produce free carriers. The difference in the values of the optical conductivity for the grown films and the theoretical values for the CaSi single crystal [Fig. 14(f)] can be also associated with the imperfection of the films and reflection losses due to the surface topography and irretrievable light loss during reflection.

The reflection spectra and optical functions for single-phase $CaSi_2$ films with different types of crystal structure (hP3-$CaSi_2$ (sample G) and hR6-$CaSi_2$ (sample H)) are shown

Fig. 15. (Color online) (a) Experimental and theoretical reflection spectra of CaSi$_2$ films in G and H samples and bulk hR6-CaSi$_2$. Spectra of (b) refractive and extinction coefficients and (c) absorption coefficient for hP3-CaSi$_2$ film. Ab initio calculations of the reflection spectra were carried out for different light polarizations ($E||xx$ and $E||zz$), both for bulk hR6-CaSi$_2$ and for an ultrathin film (5.57 nm).

in Fig. 15 along with results of first-principles calculations. Taking into account that the thickness of the CaSi$_2$ film in sample H was 382 nm according to TEM data [Fig. 6(b)], while for the film in sample G it was only 15 nm [Fig. 4(a)], we could only perform calculations for a thin film (sample G). The film thickness primarily affected the reflection and absorption spectra [Figs. 15(a) and 15(c)]. The plasma minimum in the reflection spectrum for a thin film has just begun to form.[26] Whereas for a thick film, the measured reflection spectrum agrees well with the data of ab initio calculations At the same time, due to the large root-mean-square roughness, the reflection coefficient for a thick film in the region of high-energy transitions greatly decreased and did not show a fine structure. Contrary, the fine structure of the peaks in the reflection spectrum for a thin film in sample G [Fig. 15(a)] is well distinguishable and practically coincides with the peak structure in the theoretical reflection spectrum, given that the experimental spectra were recorded for unpolarized radiation. Calculations of optical functions for a thin hP3-CaSi$_2$ film have shown that the refractive index spectrum [Fig. 15(b)] is characterized by a slight change down to 0.3 eV followed by a sharp drop at 0.2 eV and an increase at smaller photon energies, which corresponds to increasing the density of states. The extinction coefficient is almost constant and small ($k = 0.2$–0.3) down to 0.3 eV and then sharply increases with decreasing photon energy. This behavior corresponds to the generation of a large number of carriers in the region of the plasma minimum. This is confirmed by the shape of the absorption coefficient spectrum [Fig. 15(c)].

For a non-single-phase sample with a certain contribution of Ca$_{14}$Si$_{19}$ on Si(111) (sample N), the reflection and transmission spectra were also recorded, and the main optical functions were calculated within the two-layer model.[54] The shape of the reflection spectrum [Fig. 16(a)] corresponds to the contribution of three types of grains that were observed in the film according to XRD data [Fig. 10(e)]: hR3-CaSi$_2$(003), CaSi(020) and Ca$_{14}$Si$_{19}$(4$\bar{2}$0). The plasma minimum in the reflection spectrum and partial transparency correlate with the data for CaSi [Fig. 14(a)] and CaSi$_2$ [Fig. 15(a)] films, but the positions of the peaks in the reflection spectrum differ somewhat from both phases. Peaks at 1.30 eV and 2.05 eV

were not observed for CaSi and CaSi$_2$. It is clearly seen a significant increase both in the refractive index and the extinction coefficient at photon energies below 0.6 and 0.2 eV [Fig. 16(b)], respectively. This issue for the extinction coefficient correlates with the behavior of the absorption coefficient spectrum [Fig. 16(c)] and optical conductivity [Fig. 16(d)], which is noticeably higher than for single-phase CaSi and CaSi$_2$ films. This suggests a higher concentration of carriers in the Ca$_{14}$Si$_{19}$ grains displaying more pronounced metallic properties compared to semimetallic CaSi and CaSi$_2$.[32,39–41]

The growth of single-phase Ca silicide films on a sapphire substrate provides a nice opportunity to estimate the real transparency of semiconductor Ca$_2$Si and semimetallic CaSi$_2$ and CaSi.[29] This is necessary to apply these silicides as translucent and conductive contacts to various photodetectors based on the silicon planar technology. As part of the study, single-phase silicide films have been grown, whose crystal structure parameters are summarized in Table I. For films with thickness of (60–95) nm the reflection (Fig. 17(a)) and transmission [Fig. 17(b)] spectra showed interference features at energies up to 2.0–3.5 eV (depending on the type of silicide) that confirms their sufficient transparency. The peaks in the reflection spectra at photon energies above 3 eV already refer to interband transitions in Ca silicides and are in good agreement with the peaks in the reflection spectra for the films of these Ca silicides on silicon [Figs. 12(a), 14(a), 15(a)]. The transmission limit at similar thicknesses is minimal [Fig. 17(b)] for the Ca$_2$Si film (2.2 eV) (sample C) and maximal for CaSi (3.8 eV) (sample F). This indicates a low density of reduced states in CaSi in the photon energy range of 0.2 up to 3.8 eV and correlates with the data of ab initio calculations [Figs. 14(c), 14(f)].

The growth of films of single-phase Ca silicides on a sapphire substrate makes it possible to estimate the real transparency of not only semiconductor Ca$_2$Si, but also semimetallic CaSi$_2$ and CaSi.[29] This is necessary in the application of these silicides as translucent and conductive contacts to various photodetectors based on silicon planar technology. As part of the study, single-phase silicide films were grown, whose crystal structure parameters are given in Table I. Registration of the reflection [Fig. 17(a)] and
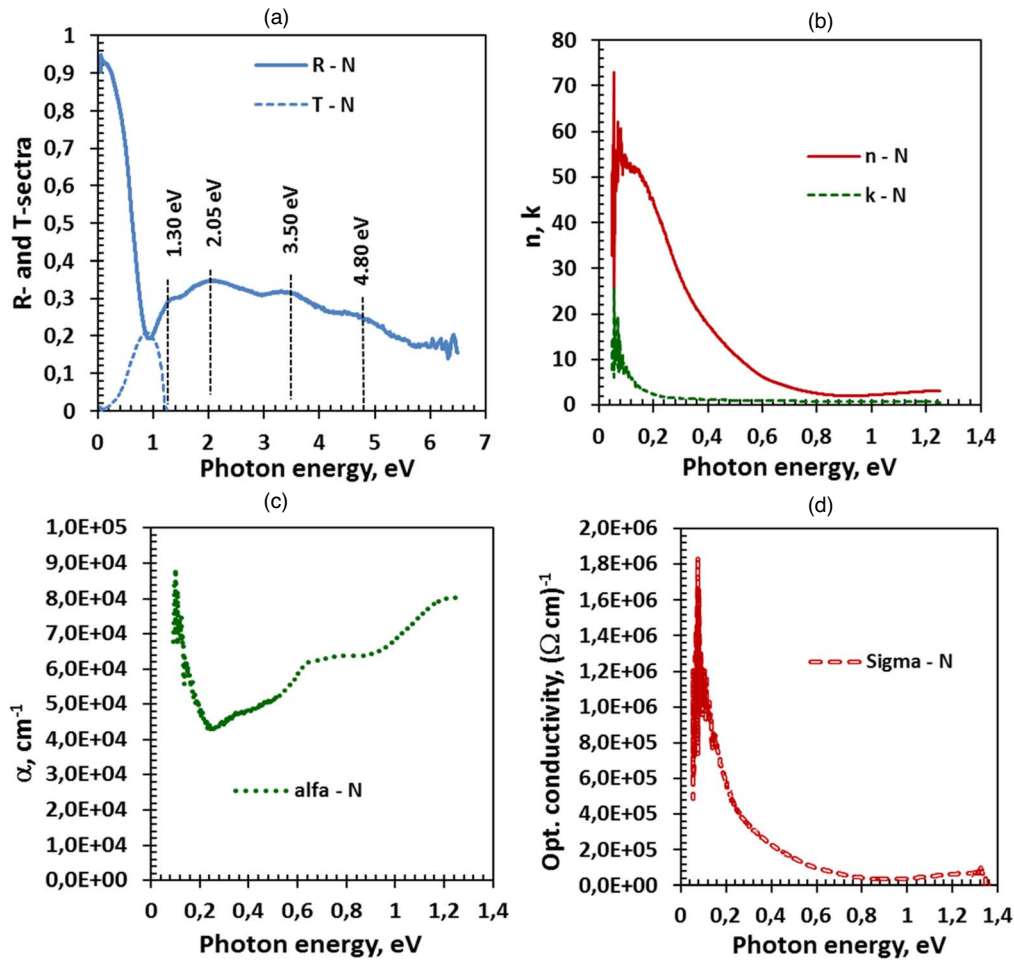
Fig. 16. (Color online) (a) Experimental reflection and transmission spectra of a film with a $Ca_{14}Si_{19}$ contribution in sample *N*. Spectra of (b) refractive and extinction coefficients, (c) absorption coefficient, and (d) optical conductivity.
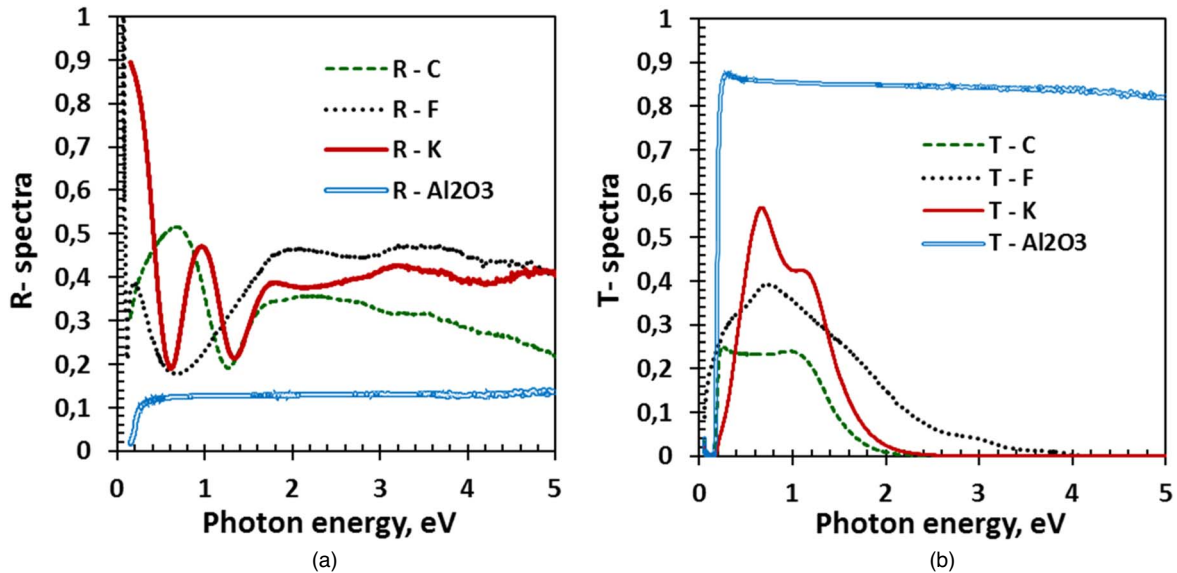
Fig. 17. (Color online) (a) Reflection and (b) transmission spectra of Ca_2Si (sample *C*), $CaSi$ (sample *F*), and $CaSi_2$ (sample *K*) films and a sapphire substrate ($Al_2O_3(0001)$).

transmission [Fig. 17(b)] spectra showed that with a film thickness of (60–95) nm, they have interference features in the reflection spectra at energies up to 2.0–3.5 eV (depending on the type of silicide), which confirms their sufficient transparency. The peaks in the reflection spectra at photon

energies above 3 eV already refer to interband transitions in the structure of Ca silicides and are in good agreement with the peaks in the reflection spectra for the films of these Ca silicides on silicon [Figs. 12(a), 14(a) and 15(a)]. The transmission limit at similar thicknesses is minimal

[Fig. 17(b)] for the Ca$_2$Si film (2.3 eV) (sample C) and maximum for CaSi (3.9 eV) (sample F), which indicates a low density of reduced states in CaSi in the photon energy range of 0.2 up to 3.9 eV and correlates with the data of ab initio calculations carried out in this work [Figs. 14(c) and 14(f)].

3.3. Photospectral properties of Ca$_2$Si/Si diode heterostructures

It is known that Ca$_2$Si is a semiconductor with the band gap ranging from 0.3–0.36 to 1.02 eV according to theoretical data.[13–16,18] However experimental results on optical spectra of Ca$_2$Si thin epitaxial films indicated a direct fundamental transition at 0.88 eV with low oscillator strength and an intense direct interband transition with an energy of 1.095 eV.[21,27] In Ca$_2$Si nanocrystals, the main contribution to absorption comes from the Urbach tail on defects at photon energies from 0.78 to 0.88 eV, but absorption at grain boundaries is observed at photon energies from 0.6 to 0.78 eV.[27] One feasible way to test the photospectral sensitivity of Ca$_2$Si semiconductor films is to form Ca$_2$Si/Si diode heterostructures and study their photoresponse. Therefore, two structures with Ca$_2$Si films on n- and p-type silicon were grown by the sacrificial-template method.[21,23] The film thickness in both samples was 70–100 nm. On each of the two halves of samples with dimensions of 5×6 mm^2, device mesa-structures were fabricated with deposited and annealed contacts to the silicide film and silicon. The contact with the substrate was formed directly to the chip body through a silver conductive paste. To control the photocurrent in the Ca$_2$Si film, an aluminum contact was attached using ultrasonic welding to a semitransparent gold film was deposited first. A photograph of a standard mesa-structure and its block diagram is shown in Fig. 18.

The current–voltage characteristics (CVC) of Ca$_2$Si/Si diode structures were studied at room temperature. On p-type silicon, a linear CVC with a very weak sensitivity to white light was found. This corresponds to the formation of a low barrier heterojunction, and the low sensitivity to light is also determined by the small thickness of the Ca$_2$Si film (70 nm). Nonlinear CVCs were observed on the Ca$_2$Si/Si-n sample, both without illumination and with illumination from a tungsten lamp. The short circuit current was 0.1–0.2 mA,
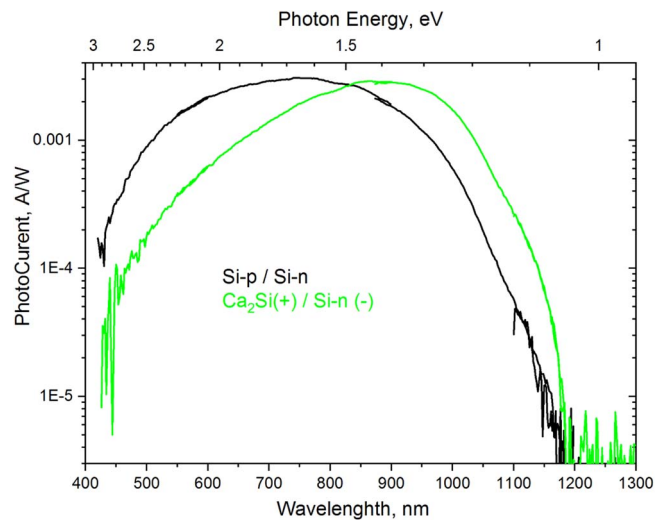
Fig. 19. (Color online) Spectral dependences of the photocurrent of Ca$_2$Si/Si-n and Si-(p–n) mesa-diodes.

and the open circuit voltage was (0.2–0.25) V, which corresponded to the formation of the Ca$_2$Si/Si-n heterojunction where the charge carriers generated by light were separated. Therefore, a Ca$_2$Si/Si-n mesa-diode was chosen to study the spectral photoresponse, and in the range 400–1300 nm photo-current spectra were recorded (Fig. 19). A mesa-diode formed on the basis of a silicon wafer with a built-in p–n junction was used as a reference. It can be seen that the spectral characteristics of the photoresponse are very similar (Fig. 19). The maximum contribution from the Ca$_2$Si/Si-n mesa-diode is observed in the photon energy range of 1.1–1.45 eV, where a smaller photoresponse is observed in the silicon diode. This is due to the fact that the Ca$_2$Si film is quite thin (up to 100 nm), so the main generation is noticeable only at energies above the band gap in Ca$_2$Si with strong absorption of radiation with energies of 1–1.48 eV. The decrease in the photoresponse from the Ca$_2$Si/Si-n mesa-diode at photon energies above 1.5 eV compared to the reference diode is associated with an increase in recombination losses in the Ca$_2$Si film due to its increased defectiveness. According to our data for the sapphire substrate, the fundamental transition in Ca$_2$Si with

(a)   (b)
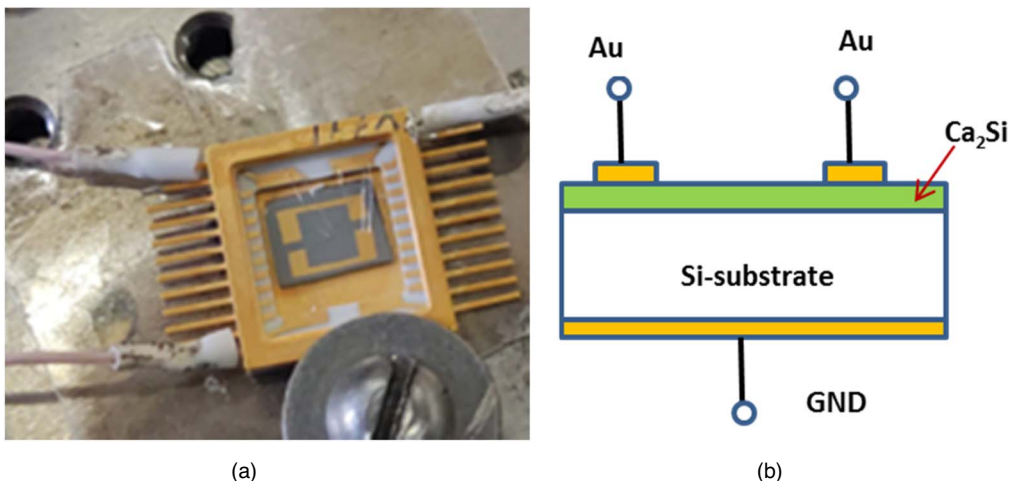
Fig. 18. (Color online) Photograph of the Ca$_2$Si/Si-p(n) diode structure in the microcircuit package (a) and a block diagram for measuring the *I–V* characteristics and photospectral characteristics of diode structures.

the negligible oscillator strength is at 0.88 eV,[27)] thus, the Ca_2Si film must be at least 1 μm thick for intense absorption of radiation and an increase in the spectral photoresponse. In this case, one can expect a noticeable generation of electron–hole pairs with energies from 0.88 to 1.5 eV and their effective separation by the Ca_2Si/Si-n heterojunction. To increase the photoresponse at photon energies above 1.5 eV, it is necessary to improve the epitaxial quality of Ca_2Si films.

4. Discussions

In this work, we present results of a comprehensive study of the crystal structure of different calcium silicides (Ca_2Si, $CaSi$, $CaSi_2$, Ca_5Si_3 and $Ca_{14}Si_{19}$) including stresses in crystal grains, their matching with silicon and sapphire, as well as a comparison of structural data and their effect on optical functions obtained from experimental data and first-principles techniques. The absence of structural data at the HRTEM level during the growth of a number of calcium silicides on silicon is critical for the development of appropriate growth technologies within the planar silicon technology. Therefore, the structural data obtained in this work are of fundamental importance.

- In Ca_2Si films, TEM and HRTEM confirmed the epitaxial growth of Ca_2Si grains in the form of vertical columns with epitaxial relationships: $Ca_2Si(100)//Si(111)$ and $Ca_2Si[010]//Si[\bar{1}12]$, which occurs from an ultrathin Mg_2Si layer. This is due to the fact that the Mg_2Si sacrificial layer formed before growth was not completely destroyed because of the low substrate temperature (300 °C, Table I) in the Ca atom's flow, as was assumed for the sacrificial seed layer approach.[23,24)] Contrary, the Mg_2Si sacrificial layer performed its orienting role and prevented the diffusion of Si atoms into the growing silicide layer, which was previously observed at relatively low temperatures (330 °C–500 °C) during the deposition of Ca atoms on silicon substrate in the form of Ca monosilicide (CaSi) as the first formed phase.[27,36,40)] As a drawback of epitaxial Ca_2Si films, one should note its low resistance to oxidation, which requires the deposition of a protective layer with high oxidation resistance after the growth process, for example, a thin layer (5 nm) of gold, chromium or semimetallic silicide with low forming temperature.
- Two types of grains with two types of epitaxial orientations were found in the CaSi film on the Si(111) substrate: $CaSi[001]||Si[\bar{1}10]$, $CaSi(220)||Si(111)$ and $CaSi[00\bar{1}]||Si[\bar{1}10]$, for which the crystal lattice parameters in the indicated planes were calculated and the distortions of these lattices were determined (in the direction of CaSi[100] compression by (−0.04% and 1.68%) and stretching in the CaSi[010] direction by (0.57% and 3.03%), respectively). Models for the two types of relationships with the silicon lattice are constructed revealing their mirror reflection with respect to each other.
- The effect of supersaturation of Ca in the Ca–Si flow on the structure of $CaSi_2$ was found during MBE growth. In epitaxial $CaSi_2$ films, two polymorphs of $CaSi_2$ crystal structure out of three existing ones were found.[46,67)] The hP3-$CaSi_2$ phase was first epitaxially formed on Si(001) during growth with low Ca supersaturation (2.25) at

$T = 500$ °C. A thick (382 nm) epitaxial and single-phase hR6-$CaSi_2$ film was formed for the first time on a Si(001) substrate at a high ratio of Ca to Si deposition rates (26.3) and a temperature of 680 °C, which indicates suppression in the accommodation coefficient decrease of Ca to Si at such high substrate temperature. A decrease in the supersaturation to 7.7 at $T = 500$ °C on Si(111) ensured the formation of an epitaxial hR6-$CaSi_2$ film, however with a significant loss in thickness due to a sharp decrease in the accommodation coefficient even at a lower substrate temperature.

- For the hP3-$CaSi_2$ film on Si(001), two types of grains with the following relationships hP3-$CaSi_2[\bar{1}00]||Si[110]$, hP3-$CaSi_2(010)||Si(002)$ and hP3-$CaSi_2[100]||Si[110]$, hP3-$CaSi_2(010)||Si(002)$ were found as well as their lattice parameters and a model of lattice matching at the interface. In the case of high Ca supersaturation and $T = 680$ °C also two types of hR6-$CaSi_2$ grains were revealed which had hR6-$CaSi_2[100]||Si[1\bar{1}0]$, hR6-$CaSi_2(01\bar{1})||Si(002)$) and hR6-$CaSi_2[100]||Si[1\bar{1}0]$, hR6-$CaSi_2(012)||Si(002)$ epitaxial relationships. The hR6-$CaSi_2(01\bar{1})$ and Si(002) planes for the first grain and the hR6-$CaSi_2(012)$ and Si(002) planes for the second grain are not strictly parallel and have the same misorientation angle between them of 3.2°. The lattice parameters of hR6-$CaSi_2$ grains, their deformations due to the Si lattice matching and models of the lattice matching at the interface were determined. During the growth of a single-phase hR6-$CaSi_2$ film on Si(111), a smooth film with epitaxial relationship hR6-$CaSi_2(006)||Si(111)$ without grains with other orientations was formed.
- For the growth of Ca_5Si_3 films, two approaches were tested: (1) MBE with an average Ca supersaturation (v_{Ca}: $v_{Si} = 3.2$) at a temperature of 400 °C on a Si(001) substrate with a gradual increase in the Ca concentration successively at three stages of Ca reactive deposition at temperatures of 490 °C, 600 °C, and 700 °C; and (2) MBE at a temperature of 470 °C and a Ca to Si deposition rate ratio of 4.0 on a sapphire substrate. In the first case, the film had a small relief with an RMS roughness of 2.3 nm and consisted of two types of crystals bounded by the $Ca_5Si_3(004)$ and CaSi(021) planes. The XRD peak from the Ca_5Si_3 phase is very narrow that indicates large sizes of crystals also in accordance with AFM data. Moreover, we suggest that CaSi, formed at $T = 400$ °C, predominantly transforms into Ca_5Si_3 in a Ca flow at temperatures of 600 °C–700 °C. The second case led to the formation of a nanocrystalline film with three types of crystals: hR6-$CaSi_2(110)$, CaSi(006), and a small amount of $Ca_5Si_3(123)$, which indicates a lack of Ca and temperature for the Ca_5Si_3 crystallization.
- The $Ca_{14}Si_{19}$ phase in the film form was first formed on Si(111) by MBE with preliminary Ca deposition (7 min) on an atomically clean silicon surface at $T = 500$ °C. According to XRD data, the film contained three types of epitaxial grains: CaSi, hR3-$CaSi_2$, and $Ca_{14}Si_{19}$. The latter consisted of $Ca_{14}Si_{19}(4\bar{2}0)$ grains formed by two perpendicular vectors: $Ca_{14}Si_{19}[120]$ and $Ca_{14}Si_{19}[001]$. It has been established that the silicide has a hexagonal

lattice (R-3m, $a = 0.86714$ nm and $c = 6.8569$ nm) and the $Ca_{14}Si_{19}[120]\|Si[1\bar{1}0]$ and $Ca_{14}Si_{19}[001]\|Si[11\bar{2}]$ epitaxial relationships. Based on the $Ca_{14}Si_{19}$ lattice parameters models of the lattice matching at the interface were proposed.

- Optical functions for the epitaxial Ca_2Si film, calculated from the reflection spectrum using the Kramers–Kronig integral relations, showed a steady increase in absorption in the film at energies above 1.7 eV and some absorption bands in the photon energy range of 0.4–1.7 eV, which may be associated with defect absorption at high defect density. The optical conductivity spectrum repeats in shape the spectrum of the absorption coefficient and indicates the decisive role in the optical conductivity of interband transitions in Ca_2Si above 2 eV. A comparison of the optical functions of the Ca_2Si film with the results of ab initio calculations for bulk Ca_2Si and its films showed a good agreement in the shape of the reflection spectra, but not in the position of the fundamental absorption edge and in the values of the absorption coefficient at photon energies from 1.2 to 1.6 eV due to roughness and dips between grains. The data of theoretical calculations for Ca_2Si films showed no noticeable changes with respect to the case of bulk Ca_2Si.

- The experimental and theoretical optical reflectance and transmittance spectra and optical functions of single-phase CaSi films and CaSi single crystals were compared. A good match of the reflection spectra in shape and amplitude was found, but small shifts were detected in the position of the plasma minimum, as well as local maxima in the region of interband transitions above 2 eV, which is due to the fact that the films are polycrystalline and contain a certain number of defects. A difference was found between the optical conductivity values for the grown CaSi films and the theoretical values for the CaSi single crystal, which is also related to the defectiveness of the films and the irretrievable loss of light upon reflection.

- Calculations of optical functions for $hP3$-$CaSi_2$ were carried out for the first time and compared with theoretical calculations of optical spectra and optical functions for $CaSi_2$ single crystal. It was shown that the fine structure of the peaks in the reflectance spectrum for a thin film is well distinguishable and practically very close to the one derived theoretically, which leads to qualitative coincidences in the optical functions compared to the theoretical optical functions.

- Calculations of optical functions with a significant contribution of the $Ca_{14}Si_{19}$ phase showed that the plasma minimum in the reflectance spectrum correlates with the data for CaSi and $CaSi_2$ films, whose grains are present in the grown film. However, the peaks at 1.30 and 2.05 eV in the reflection spectra are attributed to the $Ca_{14}Si_{19}$ phase, since they were not observed in the other two phases earlier. The sharp increase in optical conductivity at photon energies below 0.2 eV is also attributed to the contribution of the $Ca_{14}Si_{19}$ phase, which exhibits more pronounced metallic properties compared to CaSi and $CaSi_2$.phases.

- We compare the optical transparency of semiconductor (Ca_2Si) and semimetallic (CaSi and $CaSi_2$) films after their ordered growth on single-crystal sapphire with high transparency up to 5.0 eV. Even though Ca_2Si is a semiconductor, the Ca_2Si film has a minimal blue boundary of the optical transparency (2.3 eV) and the maximal limit of optical transparency (3.9 eV) has the CaSi film, which is associated with the features of its electronic structure and correlates with the data of theoretical calculations performed in this work.

- For the Ca_2Si/Si-n mesa-diode, a maximal spectral response was found in the photon energy range of 1.1–1.48 eV due to the small (up to 100 nm) thickness of the Ca_2Si film and the Ca_2Si band gap of 0.88 eV. Noticeable generation of electron–hole pairs with energies from 0.88 to 1.5 eV and their effective separation by the Ca_2Si/Si-n heterojunction can be expected at a Ca_2Si film thickness of at least 1 μm.

5. Conclusions

In this work, we discussed possible ways to fabricate single-phase films of semiconductor (Ca_2Si) and semimetallic (CaSi and $CaSi_2$) calcium silicides, as well as films with a significant contribution of Ca_5Si_3 and $Ca_{14}Si_{19}$ silicides on single-crystal silicon and sapphire substrates. Using high-resolution transmission microscopy on cross-sections and/or X-ray diffraction, the crystal structures, the unit cell parameters, epitaxial relationships with substrates were found for all grown Ca silicide films. Models of structural matching with silicon substrates were constructed for Ca_2Si, CaSi, $CaSi_2$ (polymorphs $hR3$-$CaSi_2$, $hR6$-$CaSi_2$//Si(001) and $hR6$-$CaSi_2$//Si(111)) and $Ca_{14}Si_{19}$. Optical functions for the grown films, including optical conductivity, were calculated from optical spectroscopy data within the framework of a two-layer model or the integrated Kramers–Kronig relations presented in comparison with the results of ab initio calculations. It has been found that a CaSi film possesses the maximal limit of optical transparency (3.8 eV) due to peculiarities in the CaSi band structure according to the data of ab initio calculations, which makes it extremely important for forming conductive optical contacts to silicon electronics devices. The transparency of single-phase films of Ca silicides decreases in the series CaSi–$CaSi_2$–Ca_2Si. It has been found that a Ca_2Si film on p-type silicon forms a heterojunction with a low barrier that is insensitive to white light. In Ca_2Si/Si-n mesa-diodes, an increased spectral photoresponse compared to a silicon photodiode was revealed in the photon energy range of 1.1–1.48 eV because of the generation of electron–hole pairs in the Ca_2Si film at energies above the Ca_2Si band gap (0.88 eV) and their subsequent separation at the heterojunction. And the reduced photoresponse at photon energies above 1.5 eV is associated with recombination losses at defects in the Ca_2Si film. We suggest increasing the thickness of the Ca_2Si film up to 1 μm to shift the absorption edge to the region below 1 eV, which is promising for silicon optoelectronics.

semiconductor nanomaterials" (Number in the system of the state order of the Ministry of Education and Science: 0202-2021-0002).

ORCID iDs

Nikolay G. Galkin https://orcid.org/0000-0003-4127-2988
Oleg V. Kropachev https://orcid.org/0000-0003-4300-0070

1) V. E. Borisenko (ed.) *Semiconducting Silicides* (Springer, Berlin, 2000) p.181.
2) A. T. Burkov, S. V. Novikov, V. V. Khovaylo, and J. Schumann, J. Alloys Compd. **691**, 89 (2017).
3) B. Zouak, R. Zirmi, M. S. Belkaid, and M. Pasquinelli, J. Electron. Mater. **48**, 2095 (2019).
4) N. Hirayama, T. Iida, K. Nishio, Y. Kogo, K. Takarabe, and N. Hamada, Jpn. J. Appl. Phys. **56**, 05DC05 (2017).
5) F. W. Clarke and P. Soc, Washington Bull. **11**, 135 (1889).
6) P. Manfrietti, M. L. Fornasini, and A. Palenzona, Intermetallics **8**, 223 (2000).
7) S. Lebegue, Phys. Rev. B **72**, 085103 (2005).
8) M. Affronte, S. Sanfilippo, M. Nunez-Regueiro, O. Laborde, S. LeFloch, P. Bordet, M. Hanfland, D. Levi, A. Palenzona, and G. L. Olcese, Physica B **284–288**, 1117 (2000).
9) O. Bisi, L. Braikovich, C. Carbone, I. Lindau, A. Iandelli, G. L. Olcese, and A. Palenzona, Phys. Rev. B **40**, 10194 (1989).
10) M. G. Gandolfi, F. Zamparini, M. D. Esposti, F. Chiellini, F. Fava, P. Fabbri, P. Taddei, and C. Prati, Mater. Sci. Eng. C **102**, 341 (2019).
11) Y. Warashina, Y. Ito, T. Nakamura, H. Tatsuoka, J. Snyder, M. Tanaka, T. Suemasu, Y. Anma, M. Shimomura, and Y. Hayakawa, e-J. Surf. Sci. Nanotechnol. **7**, 129 (2009).
12) T. Terada, T. Ishibe, T. Katayama, K. Sato, T. Q. Nguyen, H. Nakano, and Y. Nakamura, Appl. Phys. Express **14**, 115505 (2021).
13) D. B. Migas, L. Miglio, V. L. Shaposhnikov, and V. E. Borisenko, Phys. Rev. B **67**, 205203 (2003).
14) J. Hu, A. Kato, T. Sadoh, Y. Maeda, K. N. Galkin, T. V. Turchin, N. G. Galkin, and H. Tatsuoka, Int. J. Mod. Phys. B **24**, 4639 (2010).
15) J. Hu, A. Kato, T. Sadoh, Y. Maeda, K. N. Galkin, T. V. Turchin, N. G. Galkin, and H. Tatsuoka, Int. J. Mod. Phys. B **24**, 3693 (2010).
16) D. B. Migas, V. O. Bogorodz, A. B. Filonov, V. L. Shaposhnikov, V. E. Borisenko, and Galkin, Jpn. J. Appl. Phys. **54**, 07JA03 (2015).
17) S. Lebegue, B. Arnaud, and M. Alouani, Phys. Rev. B **72**, 085103 (2005).
18) D. B. Migas, V. L. Shaposhnikov, A. B. Filonov, N. N. Dorozhkin, and V. E. Borisenko, J. Phys. Cond. Matter **19**, 346207 (2007).
19) C. Wen et al., Phys. Proc. **11**, 106 (2011).
20) N. Takagi, Y. Sato, T. Matsuyama, H. Tatsuoka, M. Tanaka, C. Fengmin, and H. Kuwabara, Appl. Surf. Sci. **244**, 330 (2005).
21) N. G. Galkin, K. N. Galkin, S. A. Dotsenko, S. A. Pyachin, and I. A. Astapov, Mater. Sci. Semicond. Process. **113**, 105036 (2020).
22) L. Dermenji, K. G. Lisunov, K. N. Galkin, D. L. Goroshko, E. A. Chusovitin, N. G. Galkin, and E. Arushanov, Solid State Phenom. **312**, 3 (2020).
23) S. A. Dotsenko, D. V. Fomin, K. N. Galkin, D. L. Goroshko, and N. G. Galkin, Phys. Proc. **11**, 95 (2011).
24) L. Dozsa, G. Molnar, Z. Zolnai, L. Dobos, B. Pecz, N. G. Galkin, S. A. Dotsenko, D. A. Bezbabny, and D. V. Fomin, J. Mater. Sci. **48**, 2872 (2013).
25) N. G. Galkin, K. N. Galkin, I. M. Chernev, O. V. Kropachev, D. L. Goroshko, S. A. Dotsenko, E. Yu. Subbotin, and D. B. Migas, Chem. Phys. Mesosc. **24**, 145 (2022).
26) J. I. Pankov, *Optical Processes in Semiconductors* (Dover Books on Physics, New York, 2010) 2nd ed., p. 22.
27) N. G. Galkin, K. N. Galkin, I. M. Chernev, O. V. Kropachev, D. L. Goroshko, E. Yu. Subbotin, and D. B. Migas, Chem. Phys. Mesosc. **24**, 33 (2022).
28) N. Siminel, K. N. Galkin, E. Arushanov, and N. G. Galkin, Vacuum **203**, 111302 (2022).
29) K. P. O'Donnel and X. Chen, Appl. Phys. Lett. **58**, 2924 (1991).
30) Z. Yang, K. P. Homewood, M. S. Finney, M. A. Harry, and J. Reeson, J. Appl. Phys. **78**, 1958 (1995).
31) R. Passler, Phys. Status Solidi b **200**, 155 (1997).
32) M. Affronte, O. Laborde, G. L. Olsece, and A. Palenzona, J. Alloys Compd. **274**, 68 (1998).
33) N. G. Galkin, K. N. Galkin, I. M. Chernev, D. L. Goroshko, E. A. Chusovitin, A. V. Shevlyagin, A. A. Usenko, and V. V. Khovaylo, Defect Diffusion Forum **386**, 3 (2018).
34) N. G. Galkin, K. N. Galkin, A. V. Tupkalo, Z. Fogarassy, and B. Pécz, J. Alloys Compd. **813**, 152101 (2020).
35) N. G. Galkin, K. N. Galkin, A. V. Tupkalo, E. Y. Subbotin, I. M. Chernev, A. V. Shevlyagin, and V. V. Khovaylo, Chem. Phys. Mesosc. **23**, 165 (2021).
36) N. G. Galkin, K. N. Galkin, S. A. Dotsenko, D. L. Goroshko, Z. Fogarassy, and B. Pécz, Mater. Chem. Phys. **253**, 123380 (2020).
37) K. Ito, T. Suemasu, and H. Nakano, Jpn. J. Appl. Phys. **57**, 120313 (2018).
38) T. Terada, Y. Uematsu, T. Ishibe, N. Naruse, K. Sato, T. Q. Nguyen, E. Kobayashi, H. Nakano, and Y. Nakamura, Adv. Mater. Interfaces **9**, 2101752 (2021).
39) A. V. Shevlyagin, N. G. Galkin, K. N. Galkin, E. Y. Subbotin, V. M. Il'yaschenko, A. V. Gerasimenko, and I. A. Tkachenko, J. Alloys Compd. **910**, 164893 (2022).
40) N. G. Galkin, K. N. Galkin, A. V. Tupkalo, E. A. Chusovitin, D. L. Goroshko, Z. Fogarassi, and B. Pecz, Jpn. J. Appl. Phys. **59**, SFFA12 (2020).
41) N. G. Galkin et al., J. Alloys Compd. **770**, 710 (2019).
42) V. H. Nguyen, D. T. Papanastasiou, J. Resende, L. Bardet, T. Sannicolo, C. Jiménez, D. Muñoz-Rojas, N. D. Nguyen, and D. Bellet, Small **20**, 2106006 (2022).
43) T. M. Barnes, M. O. Reese, J. D. Bergeson, B. A. Larsen, J. L. Blackburn, M. C. Beard, J. Bult, and J. van de Lagemaat, Adv. Energy Mater. **2**, 353 (2012).
44) T. Inaba, A. Kato, K. Miura, M. Akasaka, T. Iida, Y. Momose, and H. Tatsuoka, Thin Solid Films **515**, 8226 (2007).
45) S. Brutti, D. Nguyen-Manh, D. G. Pettifor, P. Manfrinetti, M. Napoletano, and F. Canepa, CALPHAD, Comput. Coupling Phase Diagr. Thermochem. **33**, 260 (2009).
46) C. Jun, Y. Yinye, L. Yi, X. Quan, and Z. Jinmin, Int. Conf. on Manipulation, Manufacturing and Measurement on the Nanoscale (3M-NANO) (Xi'an, China), 2012, 75−79.
47) A. Currao, S. Wengert, R. Nesper, J. Curda, and H. Hillebrecht, J. Inorg. General Chem. **622**, 501 (1996).
48) F. Canepa, M. Napoletano, P. Manfrinetti, and A. Palenzona, J. Alloys Compd. **299**, 20 (2000).
49) A. Moll, R. Viennois, P. Hermet, A. Haidoux, J.-L. Bantignies, and M. Beaudhuin, Acta Mater. **125**, 490 (2017).
50) S. A. Dotsenko, K. N. Galkin, D. A. Bezbabny, D. L. Goroshko, and N. G. Galkin, Phys. Proc. **23**, 41 (2012).
51) N. G. Galkin, D. A. Bezbabnyi, K. N. Galkin, S. A. Dotsenko, E. Zielony, R. Kudrawiec, and J. Misiewicz, Phys. Status Solidi C **10**, 1819 (2013).
52) N. G. Galkin, D. A. Bezbabnyi, S. A. Dotsenko, K. N. Galkin, I. M. Chernev, E. A. Chusovitin, P. Nemes-Icze, L. Dozsa, and B. Pecz, Solid State Phenom. **213**, 71 (2014).
53) R. Yaokawa, A. Nagoya, and H. Nakano, J. Solid State Chem. **295**, 121919 (2021).
54) N. G. Galkin, A. M. Maslov, and A. V. Konchenko, Thin Solid Films **311**, 230 (1997).
55) G. Kresse and J. Hafner, Phys. Rev. B **47**, 558 (1993).
56) G. Kresse and J. Furthmller, Comput. Mater. Sci. **6**, 15 (1996).
57) G. Kresse and J. Furthmller, Phys. Rev. B **54**, 11169 (1996).
58) G. Kresse and D. Joubert, Phys. Rev. B **59**, 1758 (1999).
59) J. P. Perdew, K. Burke, and M. Ernzerhof, Phys. Rev. Lett. **77**, 3865 (1996).
60) J. Paier, R. Hirschl, M. Marsman, and G. Kresse, J. Chem. Phys. **122**, 234102 (2005).
61) J. Heyd, G. E. Scuseria, and M. Ernzerhof, J. Chem. Phys. **118**, 8207 (2003).
62) J. Heyd, G. E. Scuseria, and M. Ernzerhof, Erratum: J. Chem. Phys. **118**, 8207 (2003).
63) J. Heyd, G. E. Scuseria, and M. Ernzerhof, Erratum: J. Chem. Phys. **124**, 219906 (2006).
64) J. Heyd and G. E. Scuseria, J. Chem. Phys. **120**, 7274 (2004).
65) J. Heyd and G. E. Scuseria, J. Chem. Phys. **121**, 1187 (2004).
66) P. Blaha, K. Schwarz, G. K. H. Madsen, D. Kvasnicka, and J. Luitz, *WIEN2k, an Augmented Plane Wave þ Local Orbitals Program for Calculating Crystal Properties* (Karlheinz Schwarz, Tech, Universitat Wien, Vienna, 2001).
67) S. Fahy and D. R. Hamann, Phys. Rev. B **41**, 7587 (1990).